Weakening of Antarctic Stratospheric Planetary Wave Activities in Early Austral Spring Since the Early 2000s: A Response to Sea Surface Temperature Trends

YIHANG HU, WENSHOU TIAN, JIANKAI ZHANG, TAO WANG, MIAN XU

Key Laboratory for Semi-Arid Climate Change of the Ministry of Education, College of Atmospheric

Sciences, Lanzhou University, China

*Correspondence to: wstian@lzu.edu.cn

1 **Abstract**

2 Using multiple reanalysis datasets and modeling simulations, the trends of

3 Antarctic stratospheric planetary wave activities in early austral spring since the early

4 2000s are investigated in this study. We find that the stratospheric planetary wave

5 activities in September have weakened significantly since 2000, which is mainly related

6 to the weakening of the tropospheric wave sources in the extratropical southern

7 hemisphere. As the Antarctic ozone also shows clear shift around 2000, the impact of

8 ozone recovery on Antarctic planetary wave activity is also examined through

9 numerical simulations. Significant ozone recovery in lower stratosphere changes the

10 atmospheric state for wave propagation to some extent, inducing a slight decrease of

11 vertical wave flux in upper troposphere and lower stratosphere (UTLS). However, the

12 changes of wave propagation environment in middle and upper stratosphere over

13 subpolar region are not significant. The ozone recovery has minor contribution to the

14 significant weakening of stratospheric planetary wave activity in September. Further

15 analysis indicates that the trend of September sea surface temperature (SST) over 20°

16 N-70°S is well linked to the weakening of stratospheric planetary wave activities. The

17 model simulations reveal that the SST trend in the extratropical southern hemisphere

18 (20°S-70°S) and the tropics (20°N-20°S) induce a weakening of wave-1 component of

19 tropospheric geopotential height in the extratropical southern hemisphere, which

20 subsequently leads to a decrease in stratospheric wave flux. In addition, both reanalysis

21 data and numerical simulations indicate that the Brewer-Dobson circulation (BDC)

22 related to wave activities in the stratosphere has also been weakening in early austral

23   spring since 2000 due to the trend of September SST in the tropics and extratropical

24   southern hemisphere.

26   ***Key words***: *Antarctic; Stratospheric planetary wave activities; Tropospheric wave*

27   *sources; Sea surface temperature*

1. Introduction

30   The stratospheric planetary wave activities have important influences on

31   stratospheric temperature (e.g., Hu & Fu, 2009; Lin et al., 2009; Li & Tian, 2017; Li et

32   al., 2018), polar vortex (e.g., Kim et al., 2014; Zhang et al., 2016; Hu et al., 2018) and

33   distribution of chemical substances (e.g., Gabriel et al., 2011; Ialongo et al., 2012;

34   Kravchenko et al., 2011; Zhang et al., 2019a). Meanwhile, the stratospheric circulation

35   modulated by planetary waves can exert impacts on tropospheric weather and climate

36   (e.g., Haigh et al., 2005; Zhang et al., 2019b) through downward control processes

37   (Haynes et al., 1991), which is useful for extended forecast by using preceding signals

38   in the stratosphere (e.g., Baldwin et al., 2001; Wang et al., 2020).

39   The planetary perturbations generated by large-scale topography, convection and

40   continent-ocean heating contrast can propagate from the troposphere to the stratosphere

41   (Charney & Drazin, 1961) and form stratospheric planetary waves. As the land-sea

42   thermal contrast in the northern hemisphere is larger than that in the southern

43   hemisphere and produces stronger zonal forcing for the genesis of stratospheric waves,

44   the majority of attention has been given to wave activities and their impacts on weather

45   and climate in the northern hemisphere (e.g., Kim et al., 2014; Zhang et al., 2016; Hu

46   et al., 2018). However, planetary wave activities in the southern hemisphere also play

47   an important role in heating the stratosphere dynamically (e.g., Hu & Fu, 2009; Lin et

48   al., 2009), which suppresses Polar Stratospheric Clouds (PSCs) formation and ozone

49   depletion (e.g., Shen et al., 2020a; Tian et al., 2017). The Antarctic sudden stratospheric

50   warming (SSW) that occurred in 2002 (e.g., Baldwin et al., 2003; Nishii & Nakamura,

51   2004; Newman & Nash, 2005) and 2019 (e.g., Yamazaki el al., 2020; Shen et al., 2020a;

52   Shen et al., 2020b) was associated with significant upward propagation of wave flux.

53   Such episodes are extraordinarily rare in the history, and the one in 2019 contributed to

54   the formation of the smallest Antarctic ozone hole on record (WMO, 2019). In addition,

55   some studies reported that wildfires in Australia at the end of 2019 are related to

56   negative phase of the Southern Annular Mode (SAM), which was induced by the

57   extended influence of the SSW event that occurred in September (Lim et al., 2019; Shen

58   et al., 2020b). In a word, the Antarctic planetary wave activities are important for the

59   stratosphere-troposphere interactions and climate system in the southern hemisphere.

60   Long-term observations in the Antarctic stratosphere show a significant ozone

61   decline from the early 1980s to the early 2000s due to anthropogenic emission of

62   chlorofluorocarbons (CFCs) (WMO, 2011) and a recovery signal since 2000s because

63   of phasing out CFCs in response to Montreal Protocol (e.g., Angell and Free, 2009;

64   Krzyścin, 2012; Zhang et al., 2014; Banerjee et al., 2020). The Antarctic stratospheric

65   ozone depletion and recovery have important impacts on climate in the southern

66   hemisphere. The ozone depletion cools the Antarctic stratosphere through reducing

absorption of radiation and leads to the strengthening of Antarctic polar vortex during

austral spring (e.g., Randel & Wu, 1999; Solomon, 1999; Thompson et al., 2011). The

anomalous circulation in the Antarctic stratosphere during austral spring exerts impacts

on tropospheric circulations (e.g., intensification of SAM index, poleward shift of

tropospheric jet position and expansion of the Hadley cell edge) in the subsequent

months (e.g., Thompson et al., 2011; Swart & Fyfe, 2012; Son et al., 2018; Banerjee et

al., 2020) and influences the distribution of precipitation and dry zone in the southern

hemisphere (e.g., Thompson et al., 2011; Barnes et al., 2013; Kang et al., 2011).

Following the healing of ozone loss in the Antarctic ozone hole since 2000s (e.g.,

Solomon et al., 2016; Susan et al., 2019), great attention has been paid on possible

impacts of ozone recovery on climate system in the southern hemisphere (e.g., Son et

al., 2008; Barnes et al., 2013; Xia et al., 2020; Banerjee et al., 2020). Son et al. (2008)

implemented the Chemistry-Climate Model Validation (CCMVal) models to predict the

response of the southern hemisphere westerly jet to stratospheric ozone recovery. Based

on the Phase 5 of Coupled Model Intercomparison Projects (CMIP5) models, Barnes et

al. (2013) proposed that the tropospheric jet and dry zone edge no longer shift poleward

during austral summer since the early 2000s due to ozone recovery. Banerjee et al.

(2020) analyzed observations and reanalysis datasets. They found that following the

ozone recovery after 2000, the increase of SAM index and the poleward shifting of

tropospheric jet position as well as the Hadley cell edge all experienced a pause. Their

results suggest that ozone depletion and recovery have made important contributions to

the climate shift that occurred around 2000 in the southern hemisphere.

89 However, some previous studies have reported zonally asymmetric warming

90 patterns in Antarctic stratosphere, which are generated by increased planetary wave

91 activities during austral spring from the early 1980s to the early 2000s (Hu & Fu, 2009;

92 Lin et al., 2009). Note that the Antarctic stratosphere was experiencing radiative cooling

93 in the same period due to ozone depletion (e.g., Randel & Wu, 1999; Solomon, 1999;

94 Thompson et al., 2011). The increase in stratospheric planetary wave activities cannot

95 be explained by ozone decline, because the acceleration of stratospheric circumpolar

96 wind caused by radiative cooling induces more wave energy to be reflected back to the

97 troposphere   (e.g.,   Andrews   et   al.,   1987;   Holton

98 et al., 2004). Hu & Fu (2009) attributed the increase in Antarctic stratospheric wave

99 activities to the SST trend from the 1980s to the 2000s. Their results indicate that in

100 addition to ozone change, other factors such as changes in SST also contribute to

101 climate change in the southern hemisphere. Moreover, the phase of Interdecadal Pacific

102 Oscillation (IPO) also changed at around 2000 (e.g., Trenberth et al., 2013). SST

103 variation influences Rossby wave propagation and tropospheric wave sources, and

104 thereby indirectly affects stratospheric wave activities (e.g., Lin et al., 2012; Hu et al.,

105 2018; Tian et al., 2017). The questions here are: (1) Has the trend of stratospheric

106 planetary wave activity in the southern hemisphere been shifting since the 2000s? (2)

107 What are the factors responsible for the trend of Antarctic stratospheric planetary wave

108 activity since the 2000s?

109 In this study, we reveal the trend of Antarctic planetary wave activity in early

110 austral spring since the 2000s based on multiple reanalysis datasets. We also conduct

111 sensitive experiments forced by linear increments of ozone and SST fields since the

112 2000s to investigate the response of Antarctic planetary activity to above two factors.

113 The remainder of the paper is organized as follows. Section 2 describes the data,

114 methods and configurations of model simulations. Section 3 presents the trends of

115 stratospheric and tropospheric wave activities in early austral spring. Section 4

116 examines the impact of ozone recovery on Antarctic stratospheric planetary wave

117 activity. Section 5 investigates the connections between the trends of SST and

118 stratospheric wave activities. Sections 6 discusses the responses of tropospheric wave

119 sources and stratospheric wave activities to SST changes based on model simulations.

120 Major conclusions and discussion are presented in Section 7.

121 ## 2. Datasets, methods and experimental configurations

122 a. Datasets

123 In this study, daily and monthly mean data extracted from the Modern-Era

124 Retrospective analysis for Research and Applications Version 2 (MERRA-2;

125 Bosilovich et al., 2015) dataset are used to calculate trends of Brewer-Dobson

126 circulation (BDC), tropospheric wave sources, and the Elisassen-Palm (E-P) flux and

127 its divergence in September. To verify the trend of stratospheric E-P flux, we also refer

128 to the results derived from the European Centre for Medium-range Weather Forecasting

129 (ECMWF) Interim Reanalysis (ERA-Interim; Dee et al., 2011) dataset, the Japanese

130 55-year Reanalysis (JRA-55; Kobayashi et al., 2015) dataset and the National Centers

131 for Environmental Prediction-Department of Energy Global Reanalysis 2 (NCEP-2;

132 Kanamitsu et al., 2002) dataset.

133   The observed total column ozone (TCO) data are extracted from SBUV v8.6

134   satellite dataset, which is a monthly and zonal mean dataset on 5° grid. Ozone data

135   derived from MERRA-2 dataset are also used to calculate TCO.

136   SST data are extracted from the Extended Reconstructed Sea Surface Temperature

137   (ERSST) dataset, which is a global monthly mean sea surface temperature dataset

138   derived from the International Comprehensive Ocean-Atmosphere Dataset (ICOADS).

139   The ERSST is on global 2°×2° grid and covers the period from January 1854 to the

140   present. We use the latest version (version 5, i.e., v5) dataset to calculate trends and

141   correlations, and produce SST forcing field for model simulations. More details about

142   this version of ERSST can be found in Huang et al. (2017).

143   In addition, the unfiltered Interdecadal Pacific Oscillation (IPO) index derived

144   from the ERSST v5 dataset is also used in this study. More detailed information about

145   the index can be found in Henley et al. (2015).

146   b. Diagnosis of wave activities and Brewer-Dobson circulation

147   Planetary wave activities are measured by E-P flux ($\vec{F} \equiv (0, F^{(\phi)}, F^{(z)})$) and its

148   divergence D_F. Their algorithms are expressed by Eqs. (1)-(3) (Andrews et al., 1987):

$$F^{(\phi)} = \rho_0 a \cos\phi (\overline{u_z} \, \overline{v'\theta'} / \overline{\theta}_z - \overline{v'u'}) \tag{1}$$

$$F^{(z)} = \rho_0 a \cos\phi \{ [f - (a\cos\phi)^{-1}(\overline{u}\cos\phi)_\phi] \overline{v'\theta'} / \overline{\theta}_z - \overline{w'u'} \} \tag{2}$$

$$D_F = \frac{\nabla \cdot \vec{F}}{\rho_0 a \cos\phi} = \frac{(a\cos\phi)^{-1} \dfrac{\partial}{\partial\phi}(F^{(\phi)}\cos\phi) + \dfrac{\partial F^{(z)}}{\partial z}}{\rho_0 a \cos\phi} \tag{3}$$

152   where u, v represent zonal and meridional components of horizontal wind, w

153   is vertical velocity, θ is potential temperature, a is the Earth radius, f is the

154 Coriolis parameter, z is geopotential height, ϕ is latitude, ρ_0 is the background air

155 density.

156 The quasi-geostrophic refractive index (RI) is used to diagnose the environment

157 of wave propagation (Chen & Robinson, 1992). Its algorithm is written as Eq. (4):

$$RI = \frac{\overline{q}_\varphi}{\overline{u}} - (\frac{k}{a\cos\varphi})^2 - (\frac{f}{2NH})^2 \tag{4}$$

159 where the zonal-mean potential vorticity meridional gradient $\overline{q}_\varphi$ is

$$\overline{q}_\varphi = \frac{2\Omega}{a}\cos\varphi - \frac{1}{a^2}[\frac{(\overline{u}\cos\varphi)_\varphi}{a\cos\varphi}]_\varphi - \frac{f^2}{\rho_0}(\rho_0\frac{\overline{u}_z}{N^2})_z \tag{5}$$

161 H, q, k, N^2 and Ω are the scale height, potential vorticity, zonal wave number,

162 buoyancy frequency, and Earth's angular frequency, respectively.

163 The Brewer-Dobson circulation driven by wave breaking in the stratosphere is

164 closely related to stratospheric wave activities. Its meridional and vertical components

165 $(\overline{v}^*, \overline{w}^*)$ and stream function ($\psi^*(p,\phi)$) are expressed by Eqs. (4)-(6) (Andrews et al.,

166 1987; Birner & Bönisch, 2011) :

$$\overline{v}^* \equiv \overline{v} - \rho_0^{-1}(\rho_0\overline{v'\theta'}/\overline{\theta}_z)_z \tag{6}$$

$$\overline{w}^* \equiv \overline{w} + (a\cos\phi)^{-1}(\cos\phi \cdot \overline{v'\theta'}/\overline{\theta}_z)_\phi \tag{7}$$

$$\psi^*(p,\phi) = \int_0^p \frac{-2\pi a \cdot \cos\phi \cdot \overline{v}^*(p'',\phi)}{g}dp'' \tag{8}$$

170 where p is the air pressure, π is the circular constant, g is the gravitational

171 acceleration.

172 In Eqs. (1)-(8), the overbar and prime denote a zonal mean and departure from the

173 zonal mean, respectively. The subscripts denote partial derivatives. The Fourier

174 decomposition is used to obtain components of Eqs. (1)-(3) with different zonal wave

175   numbers. Meanwhile, the Fourier decomposed components of geopotential height zonal

176   deviations are also used to determine tropospheric wave sources.

177   c. Statistical methods

178   The trend is measured by the slope of linear regression based on the least square

179   estimation. The correlation is used to analyze statistical links between different

180   variables. In this paper, all the time series have been linearly detrended before

181   calculating correlation coefficients (r) and their corresponding significances.

182   The change-point testing (e.g. Banerjee et al., 2020) is used to make sure the

183   significance of trend or correlation coefficient is not unduly influenced by some

184   particular beginning or ending years, and thereby confirm that the trend exists

185   objectively.

186   We use two-tailed student's t test to calculate the significances of trend, correlation

187   coefficient or mean difference. The result of significance test is measured by p value or

188   confidence intervals in this paper. $p \leq 0.1$, $p \leq 0.05$ and $p \leq 0.01$ suggest the trend,

189   correlation coefficient or mean difference is significant at/above the 90%, 95% and 99%

190   confidence levels, respectively. The confidence interval of trend is shown in (7) (Shirley

191   et al., 2004):

192
$$[\hat{b} - t_{1-\alpha/2}(n-2)\hat{\sigma}_b, \hat{b} + t_{1-\alpha/2}(n-2)\hat{\sigma}_b] \tag{7}$$

193   where $\hat{b}$ is estimated value of slope, $\hat{\sigma}_b$ is standard error of slope and it is written as:

194    $\hat{\sigma}_b = \hat{b} \cdot \sqrt{\dfrac{\frac{1}{r^2} - 1}{n-2}}$, $t_{1-\alpha/2}(n-2)$ denotes the value of t-distribution with the degree of

195   freedom equal to $n-2$ and the two-tailed confidence level equal to $1-\alpha$ ($\alpha = 0.90$,

196 0.95 or 0.99). The confidence interval of mean difference is expressed by Eq. (8)

197 (Shirley et al., 2004):

198 $$[\bar{X} - \bar{Y} - t_{1-\alpha/2}(M+N-2) \cdot S_w \cdot \sqrt{\frac{1}{M}+\frac{1}{N}}, \bar{X} - \bar{Y} + t_{1-\alpha/2}(M+N-2) \cdot S_w \cdot \sqrt{\frac{1}{M}+\frac{1}{N}}] \qquad (8)$$

199 where

200 $$S_w = \sqrt{\frac{1}{M+N-2}[\sum_{i=1}^{M}(X_i - \bar{X})^2 + \sum_{j=1}^{N}(Y_j - \bar{Y})^2]} \qquad (9)$$

201 Here, $\bar{X}$ and $\bar{Y}$ are the sample averages, M and N are the numbers of sample

202 sizes with two populations, $t_{1-\alpha/2}(M+N-2)$ denotes the value of t-distribution with

203 the degree of freedom equal to $M+N-2$ and the two-tailed confidence level equal to

204 $1-\alpha$.

205   Previous studies have indicated that SST impact on the stratosphere shows a

206 spatial dependence (e.g., Xie et al., 2020). To find out a robust relationship between the

207 trend of SST in a specific region and the trend of stratospheric wave activities, we divide

208 the global ocean into three regions: SH (the extratropical southern hemisphere, 70°S-

209 20°S), TROP (the tropics, 20°S-20°N) and NH (the extratropical northern hemisphere,

210 20°N-70°N). Since the impacts in different regions might be combined, we also

211 consider three combined regions named as SHtrop (the extratropical southern

212 hemisphere and the tropics, 70°S-20°N), NHtrop (the extratropical northern hemisphere

213 and the tropics, 20°S-70°N) and the Globe (70°S-70°N). To find statistical connections

214 between the trend of SST and that of stratospheric wave activities, we examine the first

215 three leading patterns (EOF1, EOF2, EOF3) and principal components (PC1, PC2, PC3)

216 of SST in above six regions obtained from Empirical Orthogonal Function (EOF)

217 analysis. In all the six regions, there is always one EOF mode that shows great similarity

218 to the spatial pattern of trend (not shown) as we do not detrend SST time series when

219 the EOF analysis is carried out. Thus, the significance of the correlation between the

220 PC time series of that EOF mode and time series of stratospheric E-P flux can be used

221 as the criterion to determine the statistical connection between the trend of SST and the

222 trend of stratospheric wave activities.

223 d. The model and experiment configurations

224   The F_2000_WACCM_SC (FWSC) component in the Community Earth System

225 Model (CESM; version 1.2.0) is used to verify the impacts of SST and ozone recovery

226 on tropospheric wave sources and stratospheric wave activities in early austral spring.

227 The FWSC component is the Whole Atmosphere Community Climate Model version 4

228 (WACCM4) with specified chemistry forcing fields (such as ozone, greenhouse gases

229 (GHG), aerosols and so on), which have fixed values in 2000 by default. The WACCM4

230 includes active atmosphere, data ocean (run as a prescribed component, simply reading

231 SST forcing data instead of running ocean model), land and sea ice. Physics schemes

232 in the WACCM4 are based on those in the Community Atmospheric Model version 4

233 (CAM4; Neale et al., 2013). The WACCM4 uses a finite-volume dynamic framework

234 and extends from the ground to approximately 145 km (5.1×10^{-6} hPa) altitude in the

235 vertical with 66 vertical levels. The simulations presented in this paper are conducted

236 at a horizontal resolution of 1.9°×2.5°. More information about the WACCM can be

237 found in Marsh et al. (2013).

238   Control experiments and sensitive experiments are conducted to investigate

239   responses of Antarctic stratospheric wave activities to SST trends and the ozone

240   recovery trend in early austral spring. For the experiments of SST trends, monthly mean

241   global SST during 1980-2000 derived from the ERSST v5 dataset is used as SST

242   forcing field in the control experiment (sstctrl). For the four sensitive experiments

243   (sstNH, sstSH, ssttrop, sstSHtrop), linear increments of SST in different regions in

244   September during 2000-2017 are used as the forcing field. Ozone, aerosols and

245   greenhouse gases (GHG) in the control experiment and the four sensitive experiments

246   all have the fixed values in 2000. For the experiments of ozone recovery trend, monthly

247   mean three-dimensional global ozone during 1980-2000 derived from the MERRA-2

248   dataset is used as the ozone forcing field in the control experiment (O3ctrl). The

249   sensitive experiment (O3sen) is forced by linear increments of ozone in September

250   during 2001-2017. The SSTs in O3ctrl and O3sen both are monthly mean global SST

251   during 1980-2000. The aerosol and greenhouse gases values in 2000 are used. These

252   experiment configurations are summarized and listed in Table 1 and Table 2.

253   Firstly, we run the FWSC component to generate randomly different initial

254   conditions for 120 years with free run. Then, each experiment includes 100 ensemble

255   members that run from July to September forced by these initial conditions from the

256   21st year to the 120th year in July. The forcing fields of SST and ozone are only

257   superposed from July to September. July and August are taken as spin-up time and

258   simulations during this period are discarded. The ensemble mean in September derived

259   from these 100 ensemble members is regarded as the final result of each experiment. A

260   similar approach is implemented for sensitive experiments, in which the forcing fields

261 superposed only in certain months. The same approach has been used in previous

262 studies (e.g., Zhang et al., 2018).

3. Trend of planetary wave activities in early austral spring

264 Figure 1 shows the trends of stratospheric planetary wave activities in the southern

265 hemisphere September during 1980-2000 and 2000-2017, respectively. Note that the

266 vertical E-P flux entering into the stratosphere over 50°S-70°S in September has been

267 increasing during 1980-2000, accompanied by intensified wave flux convergence in the

268 upper stratosphere (Fig. 1a) that is mainly contributed by the wave-1 component (Fig.

269 1b). This feature implies that the stratospheric planetary wave activities have

270 strengthened in early austral spring during 1980-2000. A similar result has been

271 reported in previous studies (Hu & Fu, 2009; Lin et al., 2009). During 2000-2017,

272 however, vertical propagation of stratospheric E-P flux weakened over the subpolar

273 region of the southern hemisphere, which was accompanied by intensified wave flux

274 divergence in the upper stratosphere (Fig. 1d) mainly contributed by the wave-1

275 component (Fig. 1e) while the wave-2 component also made certain contributions (Fig.

276 1f). Similar features also appear in August, but not as significant as that in September

277 (Fig. S1). For this reason, hereafter we focus on the features in September.

278 The SSW that occurred in 2002 was accompanied with large upward wave fluxes

279 in the stratosphere, which is extremely rare in history and has been studied extensively

280 in previous studies (e.g., Baldwin et al., 2003; Nishii & Nakamura, 2004; Newman &

281 Nash, 2005). Since the period with a negative trend of stratospheric vertical wave flux

282 is short, it is necessary to further investigate whether such a negative trend is artificially

283   influenced by the single year of 2002. Therefore, following Banerjee et al. (2020), we

284   use a change-point method to test the significance of the trend during various periods

285   based on four reanalysis datasets (ERA-Interim, MERRA-2, JRA-55, NCEP-2).

286   Figures 2a (including the year 2002) and 2b (excluding the year 2002) display the time

287   series of area-weighted vertical stratospheric wave flux (Fz) over the southern

288   hemisphere subpolar region obtained from different reanalysis datasets. Note that the

289   wave flux time series obtained from the four reanalysis datasets all present a positive

290   trend from the early 1980s to the early 2000s and a negative trend from the early 2000s

291   to present, regardless of whether the extreme value in 2002 is removed or not. The

292   correlation coefficients of the time series between these reanalysis datasets are above

293   0.9 and statistically significant (Table 3), suggesting that the time series derived from

294   different datasets are consistent with each other. Figures 2c-f show the trends and

295   corresponding confidence intervals calculated with four different beginning years (1980,

296   1981, 1982, 1983), four different ending years (2015, 2016, 2017, 2018), and change-

297   point years from 1998 to 2013. The trends and confidence intervals in Figures 2g-j are

298   the same as that in Figures 2c-f, except that the extreme value in 2002 is removed. The

299   positive trend from the early 1980s to the 21st century remains significant regardless of

300   different beginning years and ending change-point years (Figs. 2c-j). However, Figures

301   2c-f and Figures 2g-j indicate that the positive value of the trend is decreasing gradually

302   when the period is prolonged, which is apparently attributed to the negative trend with

303   the beginning change-point year of around 2000. Although the negative trend from the

304   change-point year to ending year becomes less significant when the value in 2002 is

305 removed, it remains significant in some periods, which are also illustrated on diagrams

306 of latitude-pressure profiles (Fig. S2). Therefore, the weakening of stratospheric wave

307 activities in early austral spring since the early 2000s is robust. In this paper, we take

308 the year 2000 as the beginning year of the weakening trend to simplify descriptions in

309 the following discussion.

310   Figure 3 shows the trends of tropospheric wave sources in September since 2000.

311 There is a significant positive trend of the wave-1 component in 500 hPa geopotential

312 height over the southern Indian ocean and a significant negative trend over the southern

313 Pacific, which form an out-of-phase superposition on its climatology (Fig. 3b). The

314 trend pattern of wave-2 component is also out-of-phase with its climatology, although

315 it is not significant (Fig. 3c). The above features still maintain when the values in 2002

316 are removed (Figs. S3b, c), implying that the southern hemispheric tropospheric wave

317 sources in early austral spring have weakened since 2000, which is also reflected in the

318 decrease of tropospheric vertical wave flux (Figs. 3d, e; Figs. S3d, e).

319 **4. Response of Antarctic stratospheric wave activity to ozone recovery**

320   Previous studies have suggested that ozone depletion and recovery are important

321 to climate shift that occurred around 2000 in the southern hemisphere during austral

322 summer (e.g., Son et al., 2008; Thompson et al., 2011; Barnes et al., 2013; Banerjee et

323 al., 2020). The impacts of stratospheric ozone changes on Antarctic wave propagation

324 during austral summer has also been examined in previous studies (e.g., Hu et al., 2015).

325 However, whether ozone recovery in September explains the weakening of

326 stratospheric planetary waves at the same month remains unclear. The correlation

327 between detrended time series of September Antarctic total column ozone (TCO)

328 derived from SBUV and stratospheric vertical wave flux (Fz) is 0.70 (p=0.0011) during

329 2000-2017. The increase of wave activity in polar stratosphere causes heating effects

330 and suppresses the formation of PSCs, and hence, slow down the ozone depletion (e.g.,

331 Shen et al. 2020a). Therefore, the Antarctic ozone and stratospheric wave activity show

332 statistically significant positive correlation. Theoretically, heating effects caused by

333 ozone recovery in Antarctic stratosphere may also decelerate the Antarctic stratospheric

334 polar vortex and induce more waves to propagate into stratosphere (Andrews et al.,

335 1987; Holton et al., 2004). These preliminary analysis cannot verify that the ozone

336 recovery is responsible for weakening of stratospheric wave activity. The role of ozone

337 recovery in stratospheric wave changes needs to be further explored by model

338 simulations. In this section, we use a group of time-slice experiments (O3ctrl and O3sen)

339 to address this issue.

340   Figure 4 shows the time series and piecewise trends of September TCO in the

341 Antarctic during 1980-2017. As reported by previous studies (e.g., Angell and Free,

342 2009; Banerjee et al., 2020; Krzyścin, 2012; Solomon et al., 2016; WMO, 2011; Zhang

343 et al., 2014), the Antarctic ozone show a significant decline during 1980-2000 (Figs. 4a,

344 b, c) and a slight recovery during 2001-2017 (Figs. 4a, d, e). The recovery trend is

345 calculated with data in 2002 removed because the large poleward transport induced by

346 SSW in 2002 leads to extreme values of ozone (e.g. Solomon et al., 2016). In addition,

347 the correlation of TCO between MERRA-2 and SBUV datasets is 0.61 (p=4.5×10^{-5}),

348 suggesting the changes of TCO derived from the reanalysis dataset and the observations

349 have a good consistency. Thus, in order to get three-dimensional structure of ozone

350 changes, the ozone data from MERRA-2 are used to make forcing fields for CESM. As

351 described in Section 2, a control experiment (O3ctrl) forced by climatological ozone

352 and a sensitive experiment forced by the linear increment of global ozone in September

353 during 2001-2017 are conducted to explore the impacts of ozone recovery. The pattern

354 of ozone forcing fields is similar to its trend patterns (Figs. 4d, e; Figs. 5a, b). Other

355 details of these two experiments have been given in Section 2 and Table 2.

356   Fig. 6 and Fig. 7 show the responses of wave activity and wave propagation

357 environment forced by O3sen. Note that the significant ozone recovery over south pole

358 mainly appears in lower stratosphere (about 200 hPa to 50 hPa) (Fig. 4e). In most

359 southern polar regions from 50 hPa to 3 hPa, the ozone recovery is not significant (Fig.

360 4e). The features are attributed to limitation of ODSs emission and reduction of

361 heterogeneous reaction on PSCs, which mainly distribute in lower stratosphere (e.g.,

362 Solomon, 1999). Ozone recovery in polar lower stratosphere absorbs more ultraviolet

363 radiation and causes cooling in Antarctic troposphere (Fig. 6b). To maintain thermal

364 balance, zonal wind accelerates below 200 hPa over 60°S-70°S (Fig. 6a).

365   The changes of zonal wind and temperature forced by ozone recovery induce

366 changes in wave propagation environment. The refractive index (RI) is a good matric

367 to reflect the atmosphere state for wave propagation. Theoretically, planetary waves

368 tend to propagate into large RI regions (Andrews et al., 1987). The responses of RI and

369 its terms are shown in Figs. 6c-f. Note that the second term of RI does not change with

370 atmospheric state and the third term of RI is insignificant compared to the first term

371   (Hu et al., 2019). Previous studies indicate that changes in zonal mean potential

372   vorticity meridional gradient $\bar{q}_\varphi$ could explain the changes in RI in middle and high

373   latitudes (e.g. Hu et al., 2019; Simpson et al., 2009). Consistent with these studies, the

374   pattern of $\bar{q}_\varphi$ show some similarity with pattern of RI (Figs. 6c, d), especially in lower

375   stratosphere over subpolar regions (Figs. 6c, d). According to the Eq. (5), the first term

376   of $\bar{q}_\varphi$ does not change with atmospheric state. Therefore, the second term

377   ($-[\dfrac{(\bar{u}\cos\varphi)_\varphi}{\cos\varphi}]_\varphi$, hereafter uyy term or barotropic term) and the third term

378   ($-\dfrac{f^2}{\rho_0}(\rho_0\dfrac{\bar{u}_z}{N^2})_z$, hereafter uzz term or baroclinic term) are investigated. Note that the

379   pattern of responses in baroclinic term is similar with $\bar{q}_\varphi$ (Figs. 6d, f). The uzz term

380   also can be written as $(\dfrac{f^2}{HN^2}+\dfrac{f^2}{N^4}\dfrac{dN^2}{dz})\bar{u}_z-\dfrac{f^2}{N^2}\bar{u}_{zz}$. Meanwhile, zonal wind

381   acceleration in upper troposphere weakens the vertical shear of u ($\bar{u}_z$) around 200 hPa

382   over subpolar regions, inducing a decrease of baroclinic term and RI in upper

383   troposphere and lower stratosphere (UTLS) over 60°S-70°S (Figs. 6d, f). The response

384   of RI induces a slight decrease of vertical wave flux in UTLS over subpolar regions

385   (Fig. 7a), which is mainly contributed by its wave-1 component (Fig. 7b). However, the

386   changes of wave activity in UTLS are not significant in ensemble mean of simulations

387   (Figs. 7a, b, c). Meanwhile, note that the responses of zonal wind and temperature to

388   ozone recovery are not significant above 50 hPa over subpolar regions (Figs. 6a, b),

389   inducing negligible changes of wave propagation environment (Fig. 6c) and wave

390   activity (Fig. 7) in middle and upper stratosphere.

391   In a word, the significant ozone recovery in Antarctic lower stratosphere changes

392 wave propagation in upper troposphere and lower stratosphere to some extent. However,

393 these weak responses still cannot explain the significant decrease of stratospheric wave

394 flux in September.

5. Role of SST trends in the weakening of Antarctic stratospheric wave activities

397   In this section, we further explore factors responsible for the weakening of

398 tropospheric wave sources and stratospheric wave activities since the early 2000s in

399 early austral spring. Many studies reported that SST variations can affect stratospheric

400 climate (e.g., Li, 2009; Hurwitz et al., 2011; Lin et al., 2012; Hu et al., 2014; Hu et al.,

401 2018; Tian et al., 2017; Xie et al., 2020). Hu & Fu (2009) also attributed the

402 strengthened stratospheric wave activities in the southern hemisphere to SST trend from

403 the early 1980s to the early 2000s. Furthermore, global SST in September during 2000-

404 2017 also has a significant trend. The significant warming pattern is mainly found over

405 the southern Indian ocean, the southern Atlantic ocean, the eastern and western

406 equatorial Pacific, the western equatorial and Northern Atlantic ocean (Fig. 8b). A

407 significant cooling pattern is located over the southeast Pacific (Fig. 8b). In addition,

408 the transitions around 2000 exist in SST time series over some regions. In the southern

409 Indian ocean, SST shows insignificant trend during 1980-2000 and significant warming

410 trend during 2000-2017 (Fig. 8c). The subtropical Pacific ocean in east of Australia is

411 linked with the Pacific-Southern America (PSA) wave train (e.g. Shen et al., 2020b),

412 and the SST there shows significant warming trend during 1980-2000 and insignificant

413 trend during 2000-2017. The SST in southeast Pacific shows insignificant trend during

414   1980-2000 and significant cooling during 2000-2017 (Fig. 8e). Trends of SST in

415   southern Atlantic ocean are opposite during these two piecewise periods, showing

416   significant cooling during 1980-2000 and significant warming during 2000-2017. It is

417   apparent that the spatial pattern of SST trend during 2000-2017 is obviously different

418   from that during 1980-2000 (Fig. 8a, b), which may affect the tropospheric wave

419   sources. Thus, it is necessary to analyze the connection between SST trend and wave

420   activity trend since the early 2000s.

421   Figure 9 shows the significance of the trend of principle component (PC) time

422   series of SST in different regions (Figs. 9a-f), and the significance of correlations (Figs.

423   9g-l) between the PC time series and Fz in September during various periods. The trend

424   of PC1 time series in SH region is significant during serval periods (Fig. 9a), while the

425   correlation between PC1 and Fz is only significant with the particular ending year of

426   2015 (Fig. 9g). This feature suggests that the connection between the SST trend in SH

427   region and the trend of stratospheric wave activity is not robust. The correlation

428   between trend of stratospheric wave activity and that of SST in TROP or NH region is

429   also weak (Fig. 9e, f). As for the combined regions, note that the PC2 time series in

430   SHtrop region has a significant trend (Fig. 9d) and the correlation between the PC2 time

431   series in SHtrop and Fz with the beginning year of around 2000 is also significant (Fig.

432   9j) regardless of different ending years. This feature implies that the extratropical

433   southern hemisphere and tropical SST has a robust connection with stratospheric wave

434   activities in early austral spring since the early 2000s. The correlations between Fz and

435   all PC time series in NHtrop (Fig. 9k) and Globe (Fig. 9l) region are not as robust as

that between Fz and PC2 time series in SHtrop region (Fig. 9j), indicating that the

connection between SST trend in extratropical northern hemisphere and the trend of

stratospheric wave activity is weak.

Figure 10 shows the first three EOF modes of September SST in SHtrop region

during 2000-2017. The second mode (Fig. 10b) shows a great similarity to the spatial

pattern of SST trend (Fig. 8b), and the corresponding PC2 time series also has a

significant trend (slope=1.71, $p<0.01$). The correlation between PC2 and Fz is

significant (r=-0.56, p=0.016) and the correlation coefficient remains significant (r=-

0.46, p=0.065) at the 90% confidence level when the value in 2002 is removed. This

result suggests that the SST trend in SHtrop region is closely related to the recent

weakening of stratospheric wave activities. The first EOF mode is similar to IPO (Fig.

10a) and its corresponding principal component is significantly correlated (r=-0.98,

$p<0.01$) with the unfiltered IPO index. However, it shows no significant trend (Fig. 10d)

and has no significant correlation (Fig. 10g) with stratospheric wave flux, implying that

the linkage between the IPO phase change at around 2000 (e.g. Trenberth et al., 2013)

and the weakening of Antarctic stratospheric wave activities is weak. The correlation

between PC3 and Fz is also not significant (Fig. 10i). Therefore, it is possible that the

combined effect of SST trend (the second EOF mode) in the tropical and extratropical

southern hemisphere leads to the weakening of stratospheric wave activities in early

austral spring since the early 2000s.

6. Simulated changes in Antarctic stratospheric wave activities forced by SST trends

458   The analysis in Section 5 suggests that the SST changes in SHtrop region may

459   contribute to the weakening of the southern hemispheric stratospheric wave activities.

460   Here, numerical experiments sstNH, sstSH, ssttrop and sstSHtrop forced by linear

461   increments of SST in September during 2000-2017 (Fig. 11; more details can be found

462   in Section 2) are conducted to verify the results presented in Section 5.

463   Figure 12 shows the simulated response of 500 hPa geopotential height to SST

464   changes in different regions. The climatological distributions of the wave-1 component

465   (Figs. 12b, e, h, k) and the wave-2 component (Figs. 12c, f, i, l) from the simulations

466   are consistent with that from reanalysis dataset (Figs. 3b, c), indicating that the model

467   can well capture spatial distributions of the atmospheric waves. Note that the wave-1

468   and wave-2 anomalies simulated with SST changes in SH, TROP and SHtrop are all

469   significant. They superpose on the corresponding climatological patterns in an out-of-

470   phase style (Figs. 12e, f, h, i, k, l), indicating that the changes in SST in SH, TROP and

471   SHtrop lead to a weakening of tropospheric wave sources in the extratropical southern

472   hemisphere. However, the predominate wave-1 component of the 500 hPa geopotential

473   height anomaly in the extratropical southern hemisphere forced by the experiment with

474   NH SST change is relatively weak (Fig. 12b). This feature suggests that the SST

475   changes in extratropical northern hemisphere are incapable of inducing a robust

476   response of tropospheric wave sources in the extratropical southern hemisphere.

477   Figure 13 shows the simulated responses of stratospheric wave activities in the

478   southern hemisphere to SST changes over different regions. It is apparent that the

479   experiments with SST changes in SH, TROP and SHtrop show significantly weakened

480   stratospheric wave activities (Figs. 13d, g, j), which are mainly attributed to the

481   responses of the wave-1 component (Figs. 13e, h, k). These results are consistent with

482   the responses of tropospheric wave sources (Figs. 12d, e, g, h, j, k). However, there are

483   no significant anomalies of stratospheric wave flux in the subpolar region in Figures

484   13a and 13b, which is consistent with the response of corresponding tropospheric wave

485   sources (Figs. 12a, b) and the weak correlation between Fz and PC time series of SST

486   in NH region (Fig. 9i). The result here suggests that the response of southern

487   hemisphere stratospheric wave activities to SST trend in NH region is weak.

488   The results of all these experiments are summarized and displayed in Figure 14,

489   which are quantified by the frequency distribution of southern hemisphere stratospheric

490   vertical wave flux derived from the 100 ensemble members of each experiment.

491   Compared to the blue fitting curves, the red fitting curves shift to the left as shown in

492   Figs. 14b, 14c and 14d, suggesting that the SST changes in SH, TROP and SHtrop

493   regions weaken the upward propagation of stratospheric wave flux. The area-weighted

494   anomalies of vertical E-P flux in the subpolar region of the southern hemisphere

495   induced by SST changes in SH, TROP and SHtrop regions are -0.084×10^5 kg·s^{-2}, -

496   0.12×10^5 kg·s^{-2} and -0.13×10^5 kg·s^{-2}, respectively. The sum of the anomalies forced by

497   sstSH and ssttrop is not equal to the anomaly forced by sstSHtrop, which may be

498   resulted from non-linear interactions between the responses of wave activities to SST

499   trends in SH region and TROP region. The weakening of stratospheric wave activities

500   forced by SST increment in the tropical region is more significant than that in

501   extratropical southern hemisphere (Figs. 14b, c, e), implying that the SST trend in the

502   tropical region contributes more to the weakening of stratospheric wave activities since

503   2000. Meanwhile, it is apparent that the weakening of the southern hemisphere

504   stratospheric wave activities forced by sstSHtrop is the most significant among all the

505   sensitive experiments (Fig. 14e). The reduction of vertical E-P flux over (50°S-70°S,

506   200 hPa-10 hPa) forced by sstSHtrop is approximately 12%. These modeling results

507   indicate that the weakening of the Antarctic stratospheric wave activities in September

508   since 2000 is induced mainly by the combined effects of SST trends in the tropical and

509   extratropical southern hemisphere. It also explains why the independent correlation

510   between Fz and PC time series obtained over SH or TROP region is not as significant

511   as that between Fz and PC time series obtained over SHtrop region (Figs. 9g, h, j).

512   Moreover, the mean linear increment of area-weighted vertical E-P flux from 200 hPa

513   to 10 hPa over 70°S-50°S in September during 2000-2017 derived from four reanalysis

514   datasets is about -0.38×10^5 kg·s^{-2}. Therefore, the contribution of SST trend over 20°N-

515   70°S (the SHtrop region) to the weakening of stratospheric activities is approximately

516   34%.

517   In addition, the reanalysis datasets show that the Brewer-Dobson circulation

518   related to wave activities in the stratosphere weakened significantly in early austral

519   spring during 2000-2017 (Fig. 15b), which is contrary to the intensified trend during

520   1980-2000 (Fig. 15a). The transition of BDC around 2000 is believed to be associated

521   with ozone depletion and recovery (e.g., Polvani et al., 2017; Polvani et al., 2018).

522   However, our modeling results suggest that the SST trend is responsible for the

523   weakening of BDC in September since 2000 (Figs. 15d, e, f), The response of BDC to

524 ozone recovery is not significant (Fig. 15c) in September, especially for the branch near

525 the Antarctic. These results indicate that apart from the ozone depletion and recovery

526 the SST trend should also be taken into consideration when exploring the mechanism

527 for the climate transition in the southern hemispheric stratosphere around 2000.

528  Previous studies reported that there is usually a time lag for tropic SST to affect

529 extratropical circulation (e.g., Shaman & Tziperman, 2011). Thus, the impact of tropical

530 SST change before September needs to be further examined. Our simulations indicate

531 that the tropical SST trend in September plays a dominate role in weakening of

532 stratospheric wave activity at the same month, and the effect of tropical SST change

533 before September is negligible compared to that in September (The detailed evidences

534 to address this issue are shown in the appendix).

535 7. Conclusions and Discussions

536  This study analyzes the trend of Antarctic stratospheric planetary wave activities

537 in early austral spring since the early 2000s based on various reanalysis datasets and

538 model simulations. Using the change-point method, we find that the Antarctic

539 stratospheric wave activities in September have been weakening significantly since

540 2000, which means the intensified trend of wave activities noted in previous researches

541 (Hu & Fu, 2009; Lin et al., 2009) are reversed after 2000 in early austral spring. Further

542 analysis suggests that the weakening of stratospheric wave activities is related to the

543 weakening of tropospheric wave sources in extratropical southern hemisphere, which

544 is mainly contributed by the wave-1 component.

545  As the Antarctic ozone also shows clear shift around the 2000, we firstly examine

546   the impact of ozone recovery on Antarctic stratospheric planetary wave activity. Our

547   simulation results indicate that significant ozone recovery in lower stratosphere changes

548   the atmospheric state for wave propagation to some extent, inducing a slight decrease

549   of vertical wave flux over UTLS region in subpolar southern hemisphere. Meanwhile,

550   the changes of wave activity in middle and upper stratosphere over subpolar region

551   induced by ozone recovery are not significant. Therefore, the ozone recovery has minor

552   contribution to the significant weakening of stratospheric planetary wave activity in

553   September.

554   EOF analysis and correlation analysis indicate that the stratospheric wave

555   activities in early austral spring during 2000-2017 are related to PC2 of SST over 20°

556   N-70°S (i.e., the SHtrop region). The corresponding EOF2 mode also shows a good

557   similarity to the spatial pattern of SST trend, suggesting that the weakening of

558   stratospheric wave activities is connected to the trend of SST in SHtrop region.

559   Meanwhile, the linkage between the SST trend in NH region and the weakening of

560   stratospheric wave activities is weak. The model simulations also support that the SST

561   changes in SHtrop region lead to a weakening of tropospheric wave sources and

562   stratospheric wave activities. The contribution of SST trend in tropical region to the

563   weakening of stratospheric wave activities is larger than that in the extratropical

564   southern hemisphere. However, the response of tropospheric wave sources and

565   stratospheric wave activities to SST trend in NH region is not osignificant. The

566   contribution of SST trend over SHtrop region to the weakening of stratospheric wave

567   activities is about 34%. Finally, both reanalysis datasets and numerical simulations

568 indicate that the Brewer-Dobson circulation related to stratospheric wave activity has

569 also been weakening in early austral spring since 2000, which is also attributed to the

570 changes of September SST in tropics and extratropical southern hemisphere.

571   Although many researchers claimed that the climate transition around 2000 in

572 southern hemisphere is related to ozone depletion and recovery (e.g., Barnes et al., 2013;

573 Banerjee et al., 2020), there is no contradiction between our results and these previous

574 studies. Firstly, the southern hemisphere tropospheric circulation (i.e., the SAM index,

575 the tropospheric jet position and the Hadley cell edge) shifts related to ozone changes

576 in these previous studies basically occurred in austral summer (e.g., Son et al, 2008;

577 Thompson et al., 2011; Barnes et al, 2013; Banerjee et al., 2020). These tropospheric

578 circulation changes are induced by downward coupling of circulation anomalies in the

579 stratosphere (e.g., Thompson et al., 2011) during October and November, when solar

580 radiation covers the entire Antarctic and causes heating effects. However, the Antarctic

581 stratospheric circulation response to ozone variation in September is not as strong as

582 that in October or November (e.g., Thompson et al., 2011, Figs. 1b, d) because solar

583 radiation can only reach part of Antarctic stratosphere during a majority period of

584 September. This implies that the response of atmospheric state in September to

585 Antarctic stratospheric ozone change is not significant. Secondly, the FWSC

586 component used in this study is an atmospheric module with prescribed SST and forcing

587 gases. Therefore, our model results only indicate that the weakening of stratospheric

588 wave activity can be attributed to SST changes, while the impact of ozone change in

589 middle and low latitudes on SST cannot be determined based on these simulations.

590   Whether the transition signal of Antarctic stratospheric ozone is stored in the ocean

591   needs more efforts to explore. This is an issue beyond the scope of this study and further

592   investigation is necessary by using a fully coupled earth system model.

593   The southern hemisphere stratospheric wave activity trend from the early 1980s to

594   the early 2000s has been examined by Hu and Fu (2009) and hence is not analyzed in

595   present study. Wang and Waugh (2012) used stratosphere-resolving chemistry-climate

596   model forced by time-varying factors to evaluate the trends of stratospheric temperature,

597   residual circulation as well as wave activity during recent decades, and the trend of

598   cumulative eddy heat flux shown in their paper is not significant (Fig. 6 in Wang and

599   Waugh (2012)). In addition, Polvani et al. (2018) used time-varying ODSs to simulate

600   Brewer-Dobson circulation and attained obvious trend transition around 2000. Their

601   simulations cover from 1960s to 2080s. The significance of simulated trend may be

602   related to model performance and the length of simulating period. As the period we

603   focus is relatively short and our purpose is attribution rather than generating a real trend,

604   we perform the ensemble time-slice experiments in this study, which are also used in

605   many other previous researches (e.g., Hu et al., 2018; Kang et al., 2011; Zhang et al.,

606   2016) to attribute trends in the atmosphere. In addition, most of the current climate

607   models cannot generate a realistic wave activity trend as waves in the atmosphere are

608   linked with various processes and factors (e.g., Baldwin & Dunkerton, 2005; Garcia &

609   Randel, 2008; Labitzke, 2005; Shindell et al., 1999; Shu et al., 2013; Xie et al., 2008).

610

611   **Data availability:**

612   The ERA-Interim is available at: https://apps.ecmwf.int/datasets/data/interim-

613   full-daily/levtype=sfc/. The MERRA-2 is available at: https://disc.gsfc.nasa.gov/d

614   atasets?keywords=%22MERRA-2%22&page=1&source=Models%2FAnalyses%20M

615   ERRA-2. The JRA-55 is available at: https://jra.kishou.go.jp/JRA-55/index_en.ht

616   ml#download. The NCEP-2 is available at: http://www.cpc.ncep.noaa.gov/product

617   s/wesley/reanalysis2/. The ERSST v5 dataset is available at: https://www1.ncdc.

618   noaa.gov/pub/data/cmb/ersst/v5/netcdf/. The observations of TCO from SBUV v

619   8.6 satellite dataset are available at: https://acd-ext.gsfc.nasa.gov/Data_services/m

620   erged/data/sbuv_v86_mod.int_lyr.70-18.za.r7.txt. The unfiltered IPO index derived

621   from ERSST v5 dataset is available at: https://psl.noaa.gov/data/timeseries/IPOT

622   PI/tpi.timeseries.ersstv5.data.

623   **Author contributions:**

624   Yihang Hu conducted experiments, produced figures and tables, organized and

625   wrote the manuscript. Wenshou Tian, Jiankai Zhang and Tao Wang contributed to revise

626   the manuscript. Mian Xu helped to design experiments.

627   **Competing interests:**

628   The authors declare that they have no competing interest.

629   **Acknowledgements:**

630   This work is supported by the National Natural Science Foundation of China

631   (41630421 and 42075062). We thank Institute Pierre Simon Laplace (IPSL), NCEP and

632   NCAR and Japan Meteorological Agency (JMA) for providing ERA-Interim, NCEP-2

633   and JRA-55 datasets. We thank National Aeronautics and Space Administration (NASA)

634   for providing MERRA-2 dataset and SBUV v8.6 satellite dataset. We thank National

635   Oceanic and Atmospheric Administration (NOAA) for providing ERSST v5 dataset and

636   IPO index. We also thank the scientific team at NCAR for providing CESM-1 model.

637   Finally, we thank the computing support provided by the Supercomputing Center and

638   the College of Atmospheric Sciences from Lanzhou University.

639

640   APPENDIX

641   **Analysis of time lag for tropical SST affects Antarctic stratospheric**

642   **wave activity**

643   As stated in the Section 2, the tropical SST anomalies (the linear inecrements) in

644   experiment ssttrop are also applied in July and August (Fig. S4) to avoid abrupt SST

645   variations from month to month, and the two months are taken as spin-up time.

646   Therefore, whether the SST forcing in July and August also contribute to the weakening

647   of Antarctic stratospheric wave activity in September or not cannot be justified based

648   on the experiment ssttrop only. Here, we performed an additional experiment

649   ssttropAug without September SST anomalies (Fig. S4f) to clarify whether the

650   weakening of Antarctic stratospheric wave activity is induced by the tropical SST trend

651   at the same month. Like other numerical experiments described in Table 1, the

652   ssttropAug also includes 100 ensemble members that run from July to September forced

653   by the same initial conditions from the 21st year to the 120th year in July generated by

654   free run. The detailed descriptions of ssttropAug and other relevant experiments in the

655   manuscript are displayed together in the Table S1 for comparison. Figure S4 shows the

656   applied global SST anomalies in ssttrop and ssttropAug from July to September.

657   The responses of tropospheric wave sources and stratospheric wave activities in

658   ssttropAug are shown in Figs. S5a-c and Figs. S5d-f, respectively. Note that the

659   anomalies of subpolar tropospheric geopotential height in September forced by changes

660   in tropical SST in August does not superpose on their climatological patterns in an

661   evident out-of-phase style (Figs. S5a-c). The anomaly of wave-1 component of

662   geopotential height shows a slight in-phase overlap with its climatology over subpolar

663   region (Fig. S5b). Accordingly, the responses of stratospheric wave activities over

664   subpolar of southern hemisphere are not significant (Figs. S5d-f). The results here

665   suggest that, the decrease of September vertical wave flux induced by SST changes in

666   August is negligible comparing to that in the experiment with anomalous SST forcing

667   in September (Figs. S5g), and the tropical SST trend in September plays a dominate

668   role in weakening of stratospheric wave activity at the same month.

669   Furthermore, we also use a linear barotropic model (LBM) (e.g., Shaman &

670   Tziperman, 2007; Shaman & Tziperman, 2011) to quantify the time scale for

671   propagation of tropical anomalies to high latitudes. The LBM are developed to solve

672   the barotropic vorticity equation, which is given as Eq. (A1):

673    $$J(\overline{\psi}, \nabla^2\psi') + J(\psi', \nabla^2\overline{\psi} + f) + \alpha\nabla^2\psi' + K\nabla^4\nabla^2\psi' = R$$

674   (A1)

675   where the Jacobian $J(A, B)$ is

676    $$J(A, B) = \frac{1}{r^2}(\frac{\partial A}{\partial \lambda}\frac{\partial B}{\partial \mu} - \frac{\partial A}{\partial \mu}\frac{\partial B}{\partial \lambda}) \qquad (A2)$$

677   the forcing function R is

$$R = -(f + \nabla^2 \overline{\psi})D \qquad (A3)$$

678

679   ψ is the streamfunction, f is the Coriolis force, α is the Rayleigh coefficient, K

680 is the diffusion coefficient, λ is the longitude, $\mu = \sin(\theta)$, θ is the latitude, r is

681 the earth's radius and D is the divergence.

682   We use the wave-1 component of streamfunction derived from ensemble mean of

683 sstctrl as the background field. In LBM, the initial anomaly is given by the divergence.

684 The divergence forcing field is limited in 40°E-140°W, 10°S-0° (Fig. S6) to ensure that

685 the tropical initial anomaly of streamfunction superpose on its background field in an

686 out-of-phase style. We set $D = -7.9 \times 10^{-7} \ s^{-1}$, which is the mean divergence over the

687 forcing region. The LBM simulated streamfunction anomalies are shown in Figs. S7b-

688 i. Note that the anomalies in tropics only take a few days to arrive the high latitudes in

689 southern hemisphere. After about four days, a stable anti-phase superposition of

690 streamfunction is well established in extratropical southern hemisphere (Figs. S7f-i).

691 These results are supported by previous studies (e.g., Shaman & Tziperman, 2011),

692 which also indicate that the horizontal propagation of anomaly in atmosphere takes a

693 few days.

694   Previous studies also reported that it takes about 4 days for wave-1 to propagate

695 from troposphere into stratosphere and 1-2 days for wave-2 (e.g., Randel, 1987). Thus,

696 the tropical oceans affect the stratosphere at mid-high latitudes with a lag of several

697 days. However, the SST forcing field applied in CESM is on monthly scale. It is

698 reasonable to use September SST trend to drive and explain the trends of extratropical

699 circulation and wave activity at the same month.

700

701 **Reference**

702 Andrews, D. G., Holton, J. R., & Leovy, C. B.: Middle atmosphere dynamics, (p. 489), San Diego,

703 Calif: Academic Press Inc, 1987.

704 Angell, J. K., & Free, M.: Ground‐based observations of the slowdown in ozone decline and onset

705 of ozone increase, J. Geophys. Res., 114(D7), D07303,

706 https://doi.org/10.1029/2008JD010860, 2009.

707 Baldwin, M., P., Dunkerton, T. J.: Stratospheric harbingers of anomalous weather regimes, Science.

708 https://doi.org/10.1126/science.1063315, 2001.

709 Baldwin, M., P., Dunkerton, T., J.: The solar cycle and stratosphere-troposphere dynamical coupling.

710 J. Atmos. Sol-Terr. Phy., 67(1-2), 71-82, https://doi.org/10.1016/j.jastp.2004.07.018, 2005.

711 Baldwin, M., Hirooka, T., O'Neill, A., Yoden, S., Charlton, A. J., Hio, Y., & Yoden, S.: Major

712 stratospheric warming in the Southern Hemisphere in 2002: Dynamical aspects of the

713 ozone hole split, SPARC Newsletter, 20, 24–26, 2003.

714 Banerjee, A., Fyfe, J. C., Polvani, L. M., Waugh D., Chang K. L.: A pause in Southern Hemisphere

715 circulation trends due to the Montreal Protocol, Nature, 579(7800), 544–548,

716 https://doi.org/10.1038/s41586-020-2120-4, 2020.

717 Birner, T., & Bönisch, H.: Residual circulation trajectories and transit times into the extratropical

718 lowermost stratosphere, Atmos. Chem. Phys., 11(2), 817–827, https://doi.org/10.5194/acp-

719 11-817-2011, 2011.

720 Bosilovich, M., Akella, S., Coy, L., Cullather, R., Draper, C., Gelaro, R. and Suarez, M.: MERRA-2:

721 Initial Evaluation of the Climate, NASA Technical Report Series on Global Modeling and Data

722   Assimilation, 43, 139, 2015.

723 Charney, J. G., & Drazin, P. G.: Propagation of planetary-scale disturbances from the lower into the

724   upper atmosphere, J. Geophys. Res., 66(1), 83-109,

725   https://doi.org/10.1029/JZ066i001p00083, 1961.

726 Dee, D. P., Uppala, S. M., Simmons, A. J., Berrisford, P., Poli, P., Kobayashi, S., et al.: The ERA‑

727   Interim reanalysis: Configuration and performance of the data assimilation system, Q. J.

728   Roy. Meteor. Soc., 137(656), 553–597, https://doi.org/10.1002/qj.828, 2011.

729 Gabriel, A., H. Körnich, Lossow, S., Peters, D. H. W., & Murtagh, D.: Zonal asymmetries in middle

730   atmospheric ozone and water vapour derived from odin satellite data 2001–2010, Atmos.

731   Chem. and Phys., 11(18), 9865-9885, https://doi.org/10.5194/acp-11-9865-2011, 2011.

732 Garcia, R. R., & Randel, W. J.: Acceleration of the brewer-dobson circulation due to increases in

733   greenhouse gases, J. Atmos. Sci., 65(8), 2731-2739.

734   https://doi.org/10.1175/2008JAS2712.1, 2008.

735 Haigh, J. D., Blackburn, M., & Day, R.: The response of tropospheric circulation to perturbations in

736   lower-stratospheric temperature, J. Climate, 18(17), 3672-3685.

737   https://doi.org/10.1175/JCLI3472.1, 2005.

738 Haynes, P. H., M. E. McIntyre, T. G. Shepherd, C. J. Marks, and K. P. Shine.: On the "Downward

739   Control" of Extratropical Diabatic Circulations by Eddy-Induced Mean Zonal Forces, J.

740   Atmos. Sci., 48(4), 651–678, https://doi.org/10.1175/1520-

741   0469(1991)048<0651:OTCOED>2.0.CO;2, 1991.

742 Holton, J.: An introduction to dynamic meteorology, (p. 535), Elsevier Academic Pr., 2004.

743 Huang, B., Peter W. Thorne, et. al.: Extended Reconstructed Sea Surface Temperature version 5

744   (ERSSTv5), Upgrades, validations, and intercomparisons, J. Climate, 30(20), 8179-

745   8205, https://doi.org/10.1175/JCLI-D-16-0836.1, 2017.

746   Hu, D., Tian, W., Xie, F., Shu, J., Dhomse, S.: Effects of meridional sea surface temperature changes

747   on stratospheric temperature and circulation, Adv. Atmos. Sci., 31, 888–900.

748   https://doi.org/10.1007/s00376-013-3152-6, 2014.

749   Hu, D., Tian, W., Xie, F., Wang, C., Zhang, J.: Impacts of stratospheric ozone depletion and recovery

750   on wave propagation in the boreal winter stratosphere, J. Geophys. Res-Atmos., 120(16),

751   8299-8317, https://doi.org/10.1002/2014JD022855, 2015.

752   Hu, D., Guan, Z., Tian, W., & Ren, R.: Recent strengthening of the stratospheric Arctic vortex

753   response to warming in the central North Pacific, Nat. Commun., 9(1), 1697.

754   https://doi.org/10.1038/s41467-018-04138-3, 2018.

755   Hu, D., Guo, Y., & Guan, Z.: Recent weakening in the stratospheric planetary wave intensity in early

756   winter, Geophys. Res. Lett., 46(7), 3953-3962, https://doi.org/10.1029/2019GL082113,

757   2019.

758   Hurwitz, M. M., Newman, P. A., Oman, L. D., & Molod, A. M.: Response of the antarctic

759   stratosphere to two types of El niño events, J. Atmos. Sci., 68(4), 812-822.

760   https://doi.org/10.1175/2011JAS3606.1, 2011.

761   Hu, Y., & Fu, Q.: Stratospheric warming in southern hemisphere high latitudes since 1979, Atmos.

762   Chem. Phys., 9(13), 4329-4340, https://doi.org/10.5194/acp-9-4329-2009, 2009.

763   Ialongo, I., Sofieva, V., Kalakoski, N., Tamminen, J., & E. Kyrölä.: Ozone zonal asymmetry and

764   planetary wave characterization during antarctic spring, Atmos. Chem. Phys., 12(5), 2603-

765   2614, https://doi.org/10.5194/acp-12-2603-2012, 2012.

766 Kanamitsu, M., Ebisuzaki, W., Woollen, J., Yang, S. K., Hnilo, J. J., Fiorino, M., & Potter, G. L.:

767   NCEP–DOE AMIP-II Reanalysis (R-2), B. Am. Meteorol. Soc., 83(11), 1631–1644.

768   https://doi.org/10.1175/BAMS-83-11-1631, 2002.

769 Kang, S. M., Polvani, L. M., Fyfe, J. C., & Sigmond, M.: Impact of polar ozone depletion on

770   subtropical precipitation, Science, 332(6032), 951-954,

771   https://doi.org/10.1126/science.1202131, 2011.

772 Kim, B. M., Son, S. W., Min, S. K., Jeong, J. H., Kim, S. J., Zhang, X., Shim, T., Yoon, J.

773   H.: Weakening of the stratospheric polar vortex by Arctic sea-ice loss, Nat.

774   Commun., 5(1), 4646, https://doi.org/10.1038/ncomms5646, 2014.

775 Kobayashi, S., Y. Ota, Y. Harada, A. Ebita, M. Moriya, H. Onoda, K. Onogi, H. Kamahori, C.

776   Kobayashi, H. Endo, K. Miyaoka, and K. Takahashi,: The JRA-55 Reanalysis: General

777   specifications and basic characteristics, J. Meteorol. Soc. of Jpn., 93(1), 5-48,

778   https://doi.org/10.2151/jmsj.2015-001, 2015.

779 Kravchenko, V. O., Evtushevsky, O. M., Grytsai, A. V., Klekociuk, A. R., Milinevsky, G. P., and

780   Grytsai, Z. I.: Quasi-stationary planetary waves in late winter Antarctic stratosphere

781   temperature as a possible indicator of spring total ozone, Atmos. Chem. Phys., 11(10),

782   28945–28967, https://doi.org/10.5194/acp-12-2865-2012, 2011.

783 Krzyścin, J. W.: Onset of the total ozone increase based on statistical analyses of global ground-

784   based data for the period 1964 – 2008, Int. J. Climatol., 32(2), 240-246,

785   https://doi.org/10.1002/joc.2264, 2012.

786 Labitzke, K.: On the solar cycle-QBO relationship: A summary. J. Atmos. Sol-Terr. Phy., 67(1-2),

787   45-54, https://doi.org/10.1016/j.jastp.2004.07.016, 2005.

788 Lin, P., Fu, Q., Solomon, S., & Wallace, J. M.: Temperature trend patterns in southern hemisphere

789   high latitudes: novel indicators of stratospheric change, J. Climate, 22(23), 6325-6341.

790   https://doi.org/10.1175/2009JCLI2971.1, 2009.

791 Lin, P., Fu, Q., & Hartmann, D.: Impact of tropical SST on stratospheric planetary waves in the

792   southern hemisphere, J. Climate, 25(14), 5030-5046. https://doi.org/10.1175/JCLI-D-11-

793   00378.1, 2012.

794 Li, S.: The influence of tropical indian ocean warming on the southern hemispheric stratospheric

795   polar vortex, Sci. China. Ser. D., 52(3), 323–332, https://doi.org/10.1007/s11430-009-

796   0029-8, 2009.

797 Li, Y., & Tian, W.: Different impact of central pacific and eastern pacific El ñino on the duration of

798   sudden   stratospheric   warming, Adv.   Atmos.   Sci.,   34(06),   771-782.

799   https://doi.org/10.1007/s00376-017-6286-0, 2017.

800 Li, Y., Tian, W., Xie, F., Wen, Z., Zhang, J., Hu, D., & Han, Y.: The connection between the second

801   leading mode of the winter North Pacific sea surface temperature anomalies and

802   stratospheric   sudden   warming   events,   Clim.   Dynam.,   51(1-2),   581-595.

803   https://doi.org/10.1007/s00382-017-3942-0, 2018.

804 Marsh, D. R., Mills, M. J., Kinnison, D. E., Lamarque, J. F., Calvo, N., & Polvani, L. M.: Climate

805   change from 1850 to 2005 simulated in CESM1 (WACCM), J. Climate, 26(19), 7372-7391.

806   https://doi.org/10.1175/JCLI-D-12-00558.1, 2013.

807 Neale, R. B., Richter, J., Park, S., Lauritzen, Lauritzen, P. H., Vavrus, S. J., Rasch, P. J., & Zhang,

808   M.:The mean climate of the community atmosphere model (cam4) in forced sst and fully

809   coupled experiments, J. Climate, 26(14), 5150-5168, https://doi.org/10.1175/JCLI-D-12-

810   00236.1, 2013.

811   Newman, P. A., & Nash, E. R.: The unusual Southern Hemisphere stratosphere winter of 2002, J.

812   Atmos. Sci., 62(3), 614–628. https://doi.org/10.1175/JAS-3323.1, 2005.

813   Nishii, K. and Nakamura, H.: Tropospheric influence on the diminished Antarctic ozone hole in

814   September   2002,   Geophys.   Res.   Lett.,   31(16),   L16103,

815   https://doi.org/10.1029/2004GL019532, 2004.

816   Polvani, L. M., Wang, L., Aquila, V., & Waugh, D. W.: The impact of ozone depleting substances

817   on tropical upwelling, as revealed by the absence of lower stratospheric cooling since the

818   late 1990s, J. Climate, 30(7), 2523-2534. https://doi.org/10.1175/JCLI-D-16-0532.1, 2017.

819   Polvani, L. M., Abalos, M., Garcia, R., Kinnison, D., & Randel, W. J.: Significant weakening of

820   Brewer-Dobson circulation trends over the 21st century as a consequence of the Montreal

821   Protocol, Geophys. Res. Lett., 45(1), 401–409, https://doi.org/10.1002/2017GL075345,

822   2018.

823   Randel, W. J.: A study of planetary waves in the southern winter troposphere and stratosphere. Part

824   I: Wave structure and vertical propagation, J. Atmos. Sci., 44(6), 917-935, 1987.

825   Randel, W. J., & Wu, F.: Cooling of the arctic and antarctic polar stratospheres due to ozone

826   depletion, J.   Climate, 12(5),   1467-1479.   https://doi.org/10.1175/1520-

827   0442(1999)012<1467:COTAAA>2.0.CO;2, 1999.

828   Shaman, J., & Tziperman, E.: An atmospheric teleconnection linking ENSO and southwestern

829   European   precipitation,   J.   Climate.,   24(1),   124-139,

830   https://doi.org/10.1175/2010JCLI3590.1, 2011.

831   Shaman, J., & Tziperman, E.: Summertime ENSO-North African-Asian Jet teleconnection and

832   implications for the Indian monsoons, Geophys. Res. Lett., 34(11), L11702, https://doi.org/

833   10.1029/2006GL029143, 2007.

834   Shen, X., Wang, L., & Osprey, S.: The southern hemisphere sudden stratospheric warming of

835   september 2019, Sci. Bull., 65(21), 1800-1802. https://doi.org/10.1016/j.scib.2020.06.028,

836   2020a.

837   Shen, X., Wang, L., & Osprey, S.: Tropospheric forcing of the 2019 antarctic sudden stratospheric

838   warming, Geophys. Res. Lett., 47(20), e2020GLO89343,

839   https://doi.org/10.1029/2020GL089343, 2020b.

840   Shindell, D., T., Miller, R., L., Schmidt, G., A., & Pandolfo, L.: Simulation of recent northern winter

841   climate trends by greenhouse-gas forcing, Nature, 399(6735), 452-455,

842   https://doi.org/10.1038/20905, 1999.

843   Shirley, D., Stanley, W., & Daniel, C.: Statistics for Research (Third Edition), (p. 627), Hoboken,

844   New Jersey: John Wiley & Sons Inc., 2004.

845   Shu, J., Tian, W., Hu, D., Zhang, J., Shang, L., Tian, Hu., & Xie, F.: Effects of the quasi-biennial

846   oscillation and stratospheric semi-annual oscillation on tracer transport in the upper

847   stratosphere. J. Atmos. Sci., 70(5), 1370-1389, https://doi.org/10.1175/JAS-D-12-053.1,

848   2013.

849   Simpson, I. R., Blackburn, M., & Haigh, J. D.: The role of eddies in driving the tropospheric

850   response to stratospheric heating perturbations, J. Atmos. Sci., 66(5), 1347-1365,

851   https://doi.org/10.1175/2008JAS2758.1, 2009.

852   Solomon, S., Ivy, D. J., Kinnison, D., Mills, M. J., Neely, R. R., & Schmidt, A.: Emergence of

853   healing in the antarctic ozone layer, Science, 353(6296), 269-274,

854   https://doi.org/10.1126/science.aae0061, 2016.

855 Solomon, S.: Stratospheric ozone depletion: a review of concepts and history, Rev. Geophys., 37(3),

856   275-316, https://doi.org/10.1029/1999RG900008, 1999.

857 Son, S. W., Han, B. R., Garfinkel, C. I., Seo-Yeon, K., Rokjin, P., & Luke, A. N., et al.: Tropospheric

858   jet response to antarctic ozone depletion: an update with chemistry-climate model initiative

859   (CCMI) models, Environ. Res. Lett., 13(5), 054024-. https://doi.org/10.1088/1748-

860   9326/aabf21, 2018.

861 Son, S. W., P. G. Edwin, K. H. Seo,: The impact of stratospheric ozone recovery on the Southern

862   Hemisphere westerly jet, Science, 320(5882), 1486-1489,

863   https://doi.org/10.1126/science.1155939, 2008.

864 Susan, E., S., Douglass, A. R., Damon, M. R.: Why do antarctic ozone recovery trends vary?, J.

865   Geophys. Res.-Atmos., 124(15), 8837-8850. https://doi.org/10.1029/2019JD030996, 2019.

866 Swart, N. C. & Fyfe, J. C.: Observed and simulated changes in the Southern Hemisphere surface

867   westerly wind-stress, Geophys. Res. Lett., 39(16), L16711,

868   https://doi.org/10.1029/2012GL052810, 2012.

869 Thompson, D., Solomon, S., Kushner, P. England, M., Grise, K. M., Karoly, D. J.: Signatures of the

870   Antarctic ozone hole in Southern Hemisphere surface climate change, Nat. Geosci., 4, 741–

871   749. https://doi.org/10.1038/ngeo1296, 2011.

872 Tian, W., Li, Y., Xie, F., Zhang, J., Chipperfield, M., & Feng, W., Hu, Y., Zhao, S., Zhou, X., Zhang,

873   Y. & Ma, X.: The relationship between lower-stratospheric ozone at southern high latitudes

874   and sea surface temperature in the east Asian marginal seas in austral spring, Atmos. Chem.

875   Phys., 17(11), 6705-6722. https://doi.org/10.5194/acp-17-6705-2017, 2017.

876   Trenberth, K. E., & Fasullo, J. T.: An apparent hiatus in global warming?, Earth's Future, 1(1), 19–

877   32, https://doi.org/10.1002/2013EF000165, 2013.

878   Wang, T., Tian, W., Zhang, J., Xie, F., Zhang, R., Huang, J. & Hu, D.: Connections between Spring

879   Arctic Ozone and the Summer Circulation and Sea Surface Temperatures over the Western

880   North Pacific, J. Climate, 33(7): 2907–2923, https://doi.org/10.1175/JCLI-D-19-0292.1,

881   2020.

882   WMO.: Scientific assessment of ozone depletion: 2010, World Meteorological Organization/United

883   Nations Environment Programme Rep. 52, 516 pp, 2011.

884   WMO.: Antarctic ozone hole is smallest on record, World Meteorological Organization. Accessed

885   October 2019 at https://public.wmo.int/en/media/news/antarctic-ozone-hole-smallest-

886   record, 2019.

887   Xia, Y., Xu, W., Hu, Y., & Xie, F.: Southern-hemisphere high-latitude stratospheric warming

888   revisit, Clim. Dynam., 54(3): 1671-1682. https://doi.org/10.1007/s00382-019-05083-7,

889   2020.

890   Xie, F., Tian, W., & Chipperfield, M., P.: Radiative effect of ozone change on stratosphere-

891   troposphere exchange. J. Geophys. Res., 113, D00B09,

892   https://doi.org/10.1029/2008JD009829, 2008

893   Xie, F., Zhang, J., Huang, Z., Lu, J., & Sun, C.: An estimate of the relative contributions of sea

894   surface temperature variations in various regions to stratospheric change, J.

895   Climate, 33(12), 4994-5011, https://doi.org/10.1175/JCLI-D-19-0743.1, 2020.

896   Yamazaki, Y., Matthias, V., Miyoshi, Y., Stolle, C., Siddiqui, T., Kervalishvili, G., et al.: September

897   2019 Antarctic sudden stratospheric warming: Quasi-6-day wave burst and ionospheric

898   effects, Geophys. Res. Lett., 47(1), e2019GL086577.

899   https://doi.org/10.1029/2019GL086577, 2020.

900   Zhang, J., Tian, W., Xie, F., Tian, H., Luo, J., Zhang, J., Liu, W., Dhomse, S.: Climate warming and

901   decreasing total column ozone over the tibetan plateau during winter and spring, Tellus B.,

902   66(1), https://doi.org/10.3402/tellusb.v66.23415, 2014.

903   Zhang, J., Tian, W. , Chipperfield, M. P. , Xie, F. , & Huang, J.: Persistent shift of the arctic polar

904   vortex towards the eurasian continent in recent decades, Nat. Clim. Change. 6, 1094–1099.

905   https://doi.org/10.1038/nclimate3136, 2016.

906   Zhang, J., Tian, W., Xie, F., Sang, W., Guo, D., Chipperfield, M., Feng, W., Hu, D.: Zonally

907   asymmetric trends of winter total column ozone in the northern middle latitudes, Clim.

908   Dynam., 52(7-8), 4483-4500, https://doi.org/10.1007/s00382-018-4393-y, 2019a.

909   Zhang, P., Wu, Y. & Smith, K. L.: Prolonged effect of the stratospheric pathway in linking Barents–

910   Kara Sea sea ice variability to the midlatitude circulation in a simplified model, Clim.

911   Dynam. 50(17), 527–539. https://doi.org/10.1007/s00382-017-3624-y, 2018.

912   Zhang, R., Tian, W., Zhang, J., Huang, J., & Xu, M.: The corresponding tropospheric environments

913   during downward-extending and nondownward-extending events of stratospheric northern

914   annual mode anomalies, J. Climate, 32(6), 1857-1873, https://doi.org/10.1175/JCLI-D-

915   18-0574.1, 2019b.

916

917   **Table 1.** Configurations of experiments for SST trends.

Experiments	Descriptions

sstctrl	Control run. Seasonal cycle of monthly mean global SST data over 1980-2000 is derived from the ERSST v5 dataset. Fixed values of ozone greenhouse gases and aerosol fields in 2000 are used.
sstNH	As in sstctrl, but with linear increments of SST in September over 2000-2017 in NH (20°N-70°N). The applied global SST anomalies are shown in Fig. 7a.
sstSH	As in sstctrl, but with linear increments of SST in September over 2000-2017 in SH (20°S-70°S). The applied global SST anomalies are shown in Fig. 7b.
ssttrop	As in sstctrl, but with linear increments of SST in September over 2000-2017 in the tropics (20°S-20°N). The applied global SST anomalies are shown in Fig. 7c.
sstSHtrop	As in sstctrl, but with linear increments of SST in September over 2000-2017 in SHtrop (20°N-70°S). The applied global SST anomalies are shown in Fig. 7d.

918   **Table 2.** Configurations of experiments for the ozone recovery trend.

Experiments	Descriptions
O3ctrl	Control run. The seasonal cycle of monthly averaged global SST data over 1980-2000 is derived from ERSST v5 dataset. The seasonal cycle of monthly mean three-dimensional global ozone over 1980-2000 is derived from MERRA-2 dataset. The GHGs and aerosol fields are specified to be fixed values in 2000.
O3sen	As in O3ctrl, but superposed with linear increments of global ozone in September over 2001-2017. The ozone data in 2002 are removed when the linear increments are calculated. The applied ozone anomalies in Southern Hemisphere are shown in Fig. S5.

919   **Table 3.** Correlations of stratospheric vertical wave flux time series (area-weighted

920   from 100 hPa to 30 hPa over 70°S-50°S) between different reanalysis dataset.

	ERA-Interim	JRA-55	MERRA-2	NCEP-2
ERA-Interim	1.00 (p=0.00)	0.99 (p<0.01)	0.98 (p<0.01)	0.93 (p<0.01)
JRA-55		1.00 (p=0.00)	0.98 (p<0.01)	0.93 (p<0.01)
MERRA-2			1.00 (p=0.00)	0.94 (p<0.01)
NCEP-2				1.00 (p=0.00)

921

922
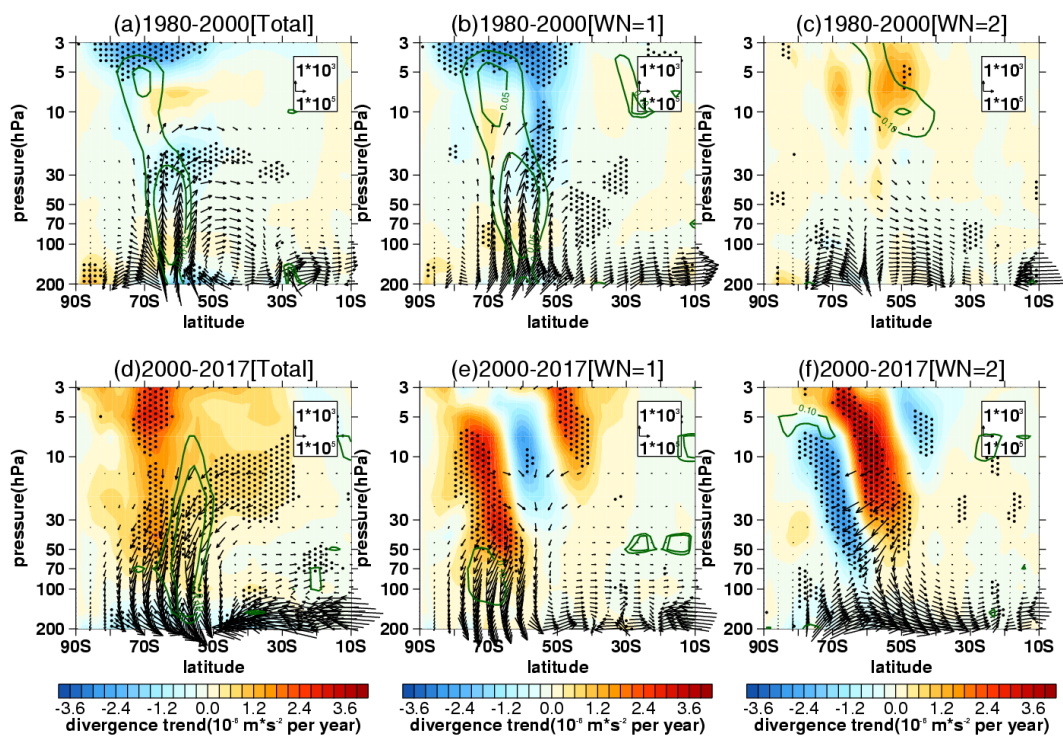
FIG. 1. Trends of southern hemisphere (a, d) stratospheric E-P flux (arrows, units of horizontal and vertical components are 10^5 and 10^3 kg·s^{-2} per year, respectively) and its divergence (shadings) with their (b, e) wave-1 components and (c, f) wave-2 components over (a, b, c) 1980-2000 and (d, e, f) 2000-2017 in September derived from MERRA-2 dataset. The stippled regions indicate the trend of E-P flux divergence significant at/above the 90% confidence level. The green contours from outside to inside (corresponding to p=0.1, 0.05) indicate the trend of vertical E-P flux significant

  at the 90% and 95% confidence level, respectively.

932
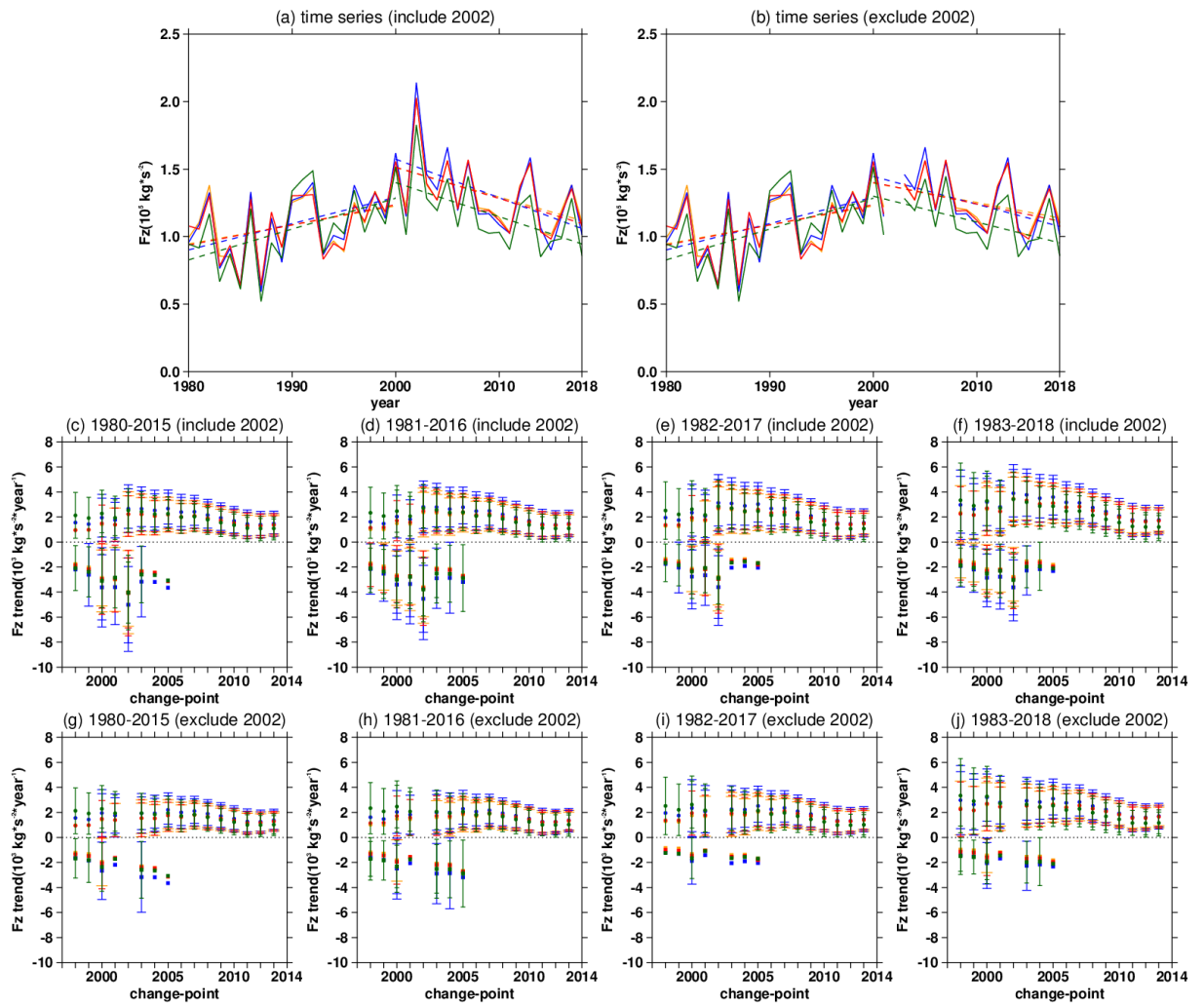
FIG. 2. (a) The mean time series (solid lines) and piecewise (during 1980-2000 and 2000-2018) linear regressions (dashed lines) of vertical E-P flux area-weighted from 100 hPa to 30 hPa over 70°S-50°S in September during 1980-2018 derived from ERA-Interim (yellow), MERRA-2 (blue), JRA-55 (red) and NCEP-2 (green). Figure (b) is the same as Figure (a), except for that the data in 2002 are removed. (c, d, e, f) The trends (dots) and uncertainties (error bars) calculated during various periods using the change-point method with different beginning and ending years (titles). Circles and

940   squares in Figures (c, d, e, f) represent positive trends from beginning years to change-

941   point years (x-axes) and negative trends from change-point years to ending years,

942   respectively. Different colors of dots and error bars in Figures (c, d, e, f) correspond to

943   colors in Figure (a), which represent trends and uncertainties derived from different

944   datasets. The long and short error bars in same color reflect the 95% and 90%

945   confidence intervals calculated by two-tailed t test. The error bar is omitted when the

946   significance of trend is lower than corresponding confidence level. Negative trends and

947   corresponding uncertainties with the beginning change-point years after 2005 are also

948   omitted, since the trend value shows large fluctuation with shortening of time series.

949   Figures (g, h, i, j) are the same as Figures (c, d, e, f), except that the data in 2002 are

950   removed when calculating trends and uncertainties.
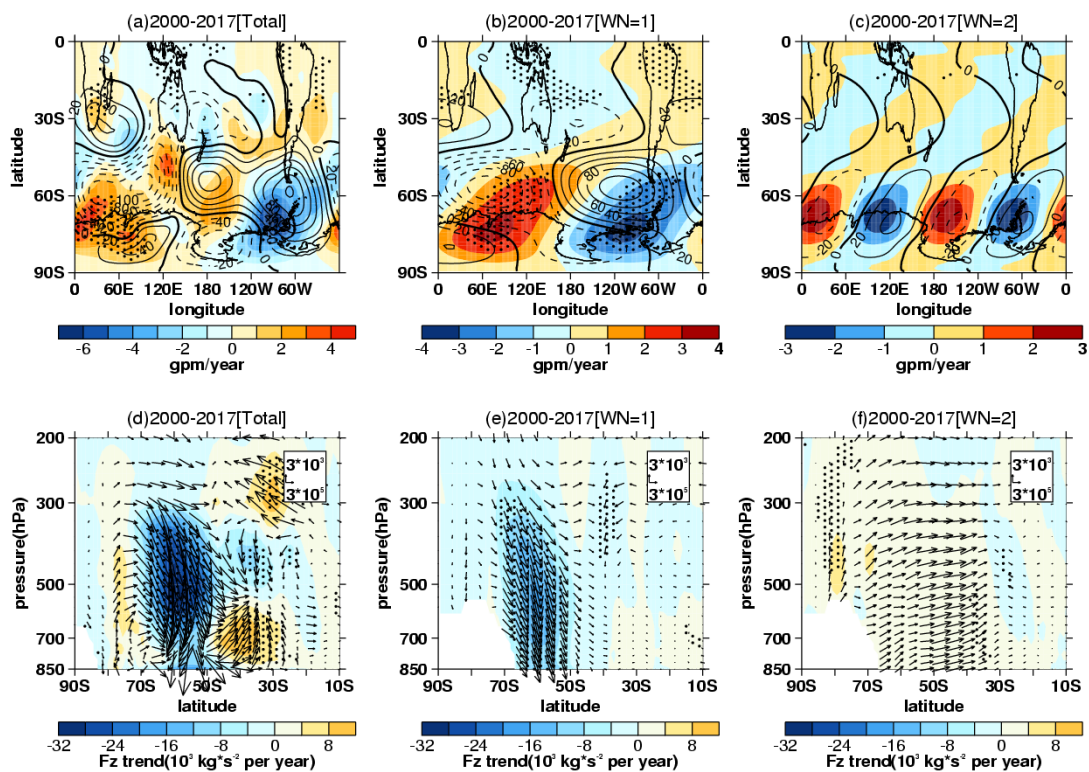
951

952   **FIG. 3.** Trends (shadings) and climatological distributions (contours with an interval

953   of 20 gpm, positive and negative values are depicted by solid and dashed lines

954 respectively, zeroes are depicted by thick solid lines) of southern hemispheric (a) 500

955 hPa geopotential height zonal deviations with their (b) wave-1 component and (c)

956 wave-2 component in September during 2000−2017 derived from MERRA-2 dataset.

957 Trends of southern hemispheric (d) tropospheric E-P flux (arrows, units of horizontal

958 and vertical components are 3×10^5 and 3×10^3 kg s^{-2} per year, respectively) and its

959 vertical component (shading) with their (e) wave-1 component and (f) wave-2

960 component in September during 2000−2017 derived from MERRA-2 dataset. The

961 stippled regions represent the trend significant at/above the 90% confidence level.

962
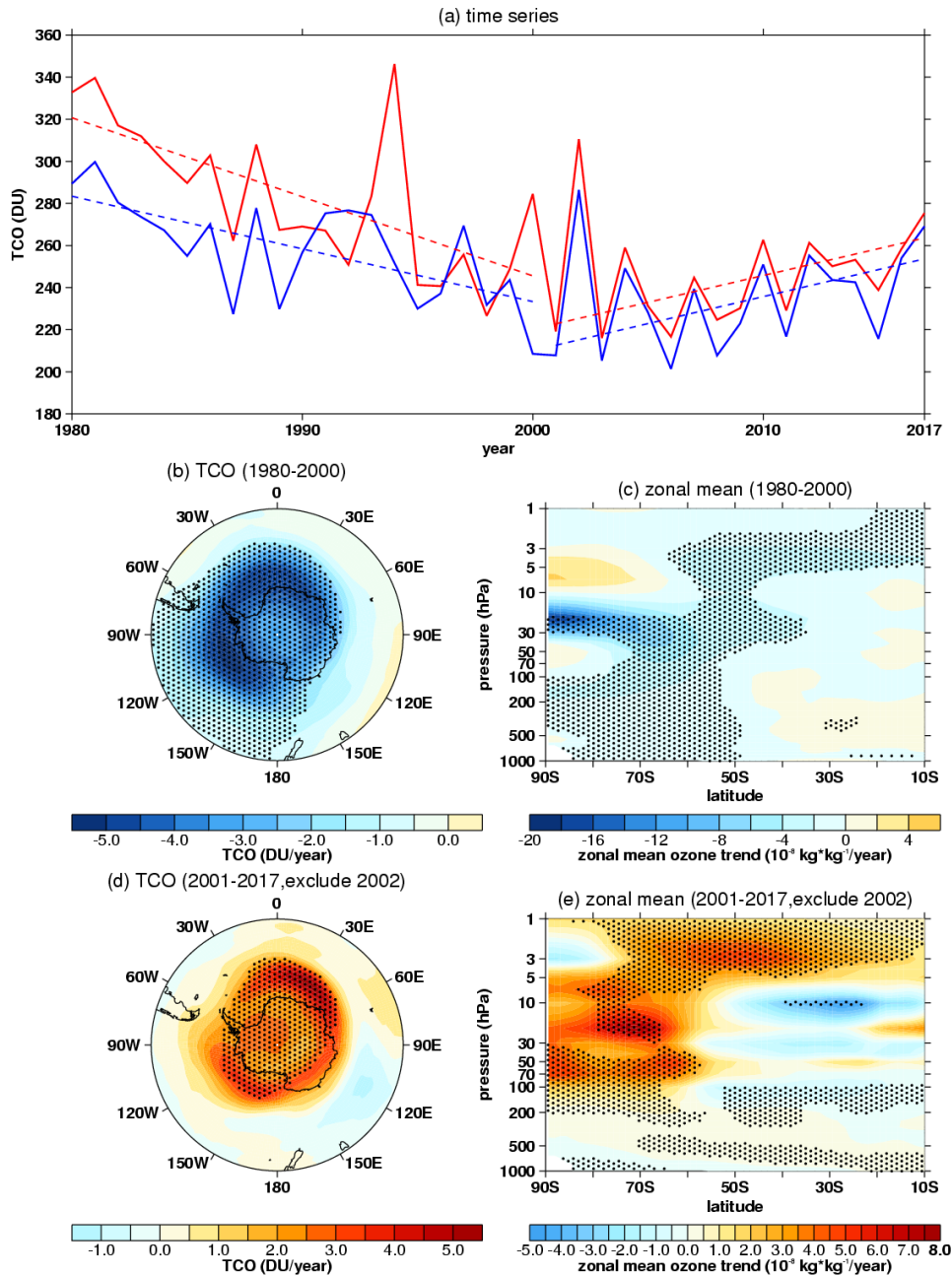
FIG. 4. (a) Time series (solid lines) of aera-weighted total column ozone (TCO) over

60°S to 90°S derived from MERRA-2 (red) and SBUV (blue) datasets. The dashed lines

represent linear regression of TCO. (b, d) The TCO trends in September during 1980-

2000 (b) and 2001-2017 (d) derived from MERRA-2 dataset. The outermost latitudes

in Figs. 4c, d are both 40°S. (c, e) The zonal mean ozone trends on latitude-pressure

profile in September during 1980-2000 (c) and 2001-2017 (e) derived from MERRA-2

969   dataset. The stippled regions in Figs. 4b-e represent trends significant at/above the 90%

970   confidence level. Data in 2002 are removed when trends, regressions and significances

971   are calculated in Fig. 4.
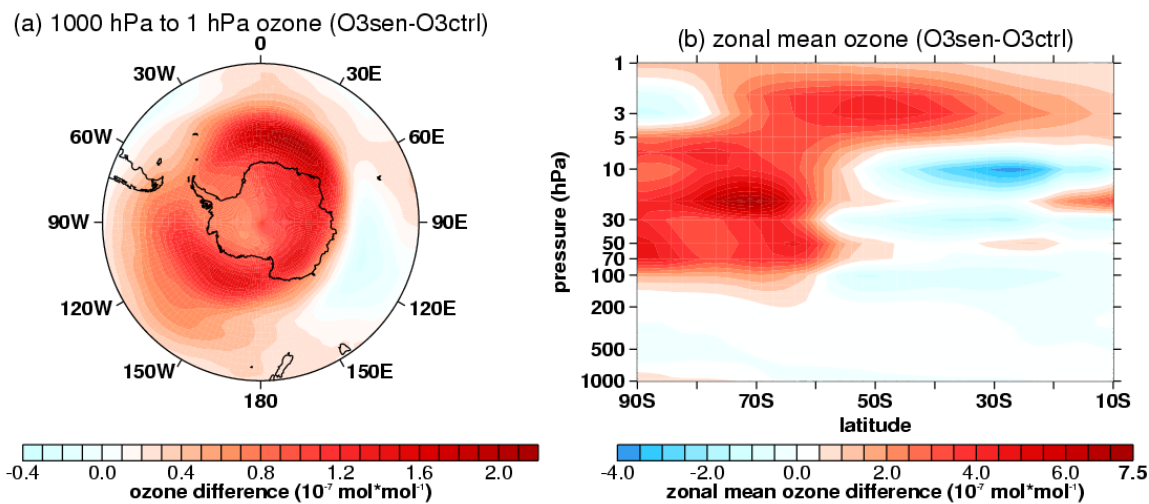
972

973   **FIG. 5.** (a) Difference of horizontal ozone forcing field averaged from 1000 hPa to 1

974   hPa between O3sen and O3ctrl. The outermost latitude in Fig. 5a is 40 ˚S. (b) Zonal

975   mean difference of ozone forcing fields on latitude-pressure profile in the southern

976   hemisphere between O3sen and O3ctrl.
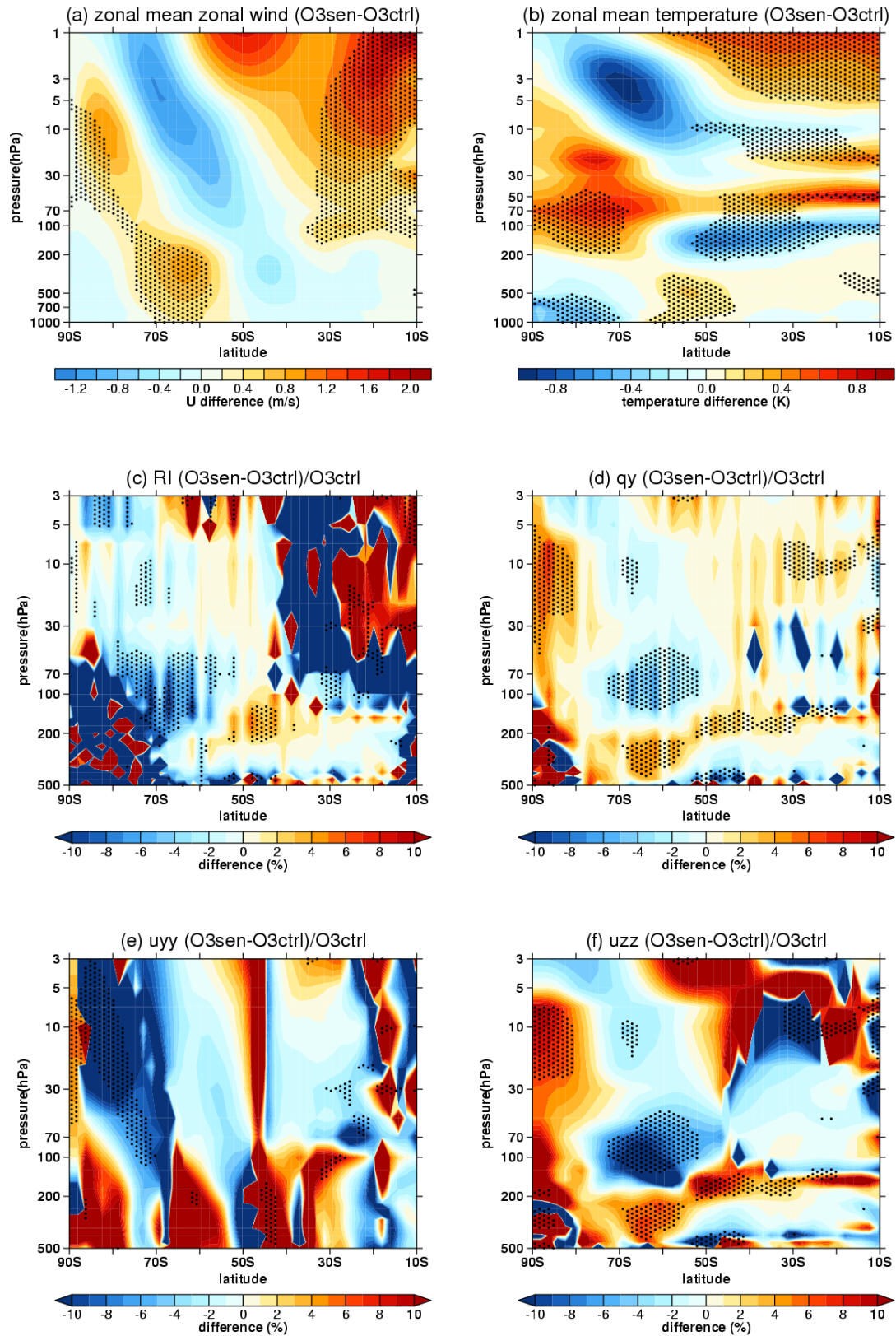
977

978 **FIG. 6**. Difference of (a) zonally averaged zonal wind, (b) zonally averaged

979   temperature, (c) refractive index, (d) $a^2 \bar{q}_\varphi$, (e) $-[\dfrac{(\bar{u}\cos\varphi)_\varphi}{\cos\varphi}]_\varphi$ (uyy term), (f)

980     $-\dfrac{a^2 f^2}{\rho_0}(\rho_0 \dfrac{\bar{u}_z}{N^2})_z$ (uzz term) between O3sen and O3ctrl. The stippled regions represent

981   the difference significant at/above 90% confidence level.
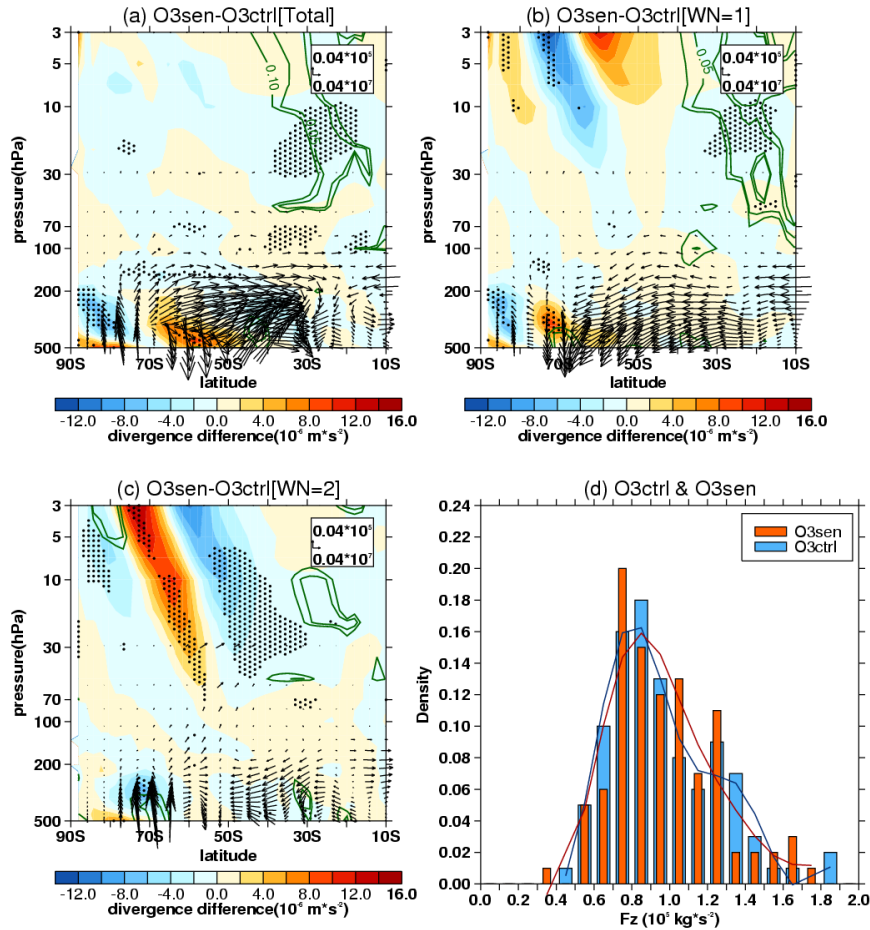
982

983   **FIG. 7.** Differences of (a) stratospheric E-P flux (arrows, units in horizontal and vertical

984   components are 0.04×10^7 and 0.04×10^5 kg s^{-2}, respectively) and its divergence

985   (shadings) with their (b) wave-1 component and (c) wave-2 component between the

986   sensitive experiment (O3sen) and the control experiment (O3ctrl). The stippled regions

987   represent the mean differences of E-P flux divergence significant at/above the 90%

988   confidence level. The green contours from outside to inside (corresponding to p=0.1,

989   0.05) represent the mean differences of vertical E-P flux significant at the 90% and 95%

990 confidence levels, respectively. (d) Frequency distributions (pillars, blue for O3ctrl and

991 orange for O3sen) of vertical E-P flux (Fz, area-weighted from 200 hPa to 10 hPa over

992 70 °S-50 °S) and it 5-point low-pass filtered fitting curves (solid lines, blue for O3ctrl

993 and red for O3sen) derived from 100 ensemble members.

994

995
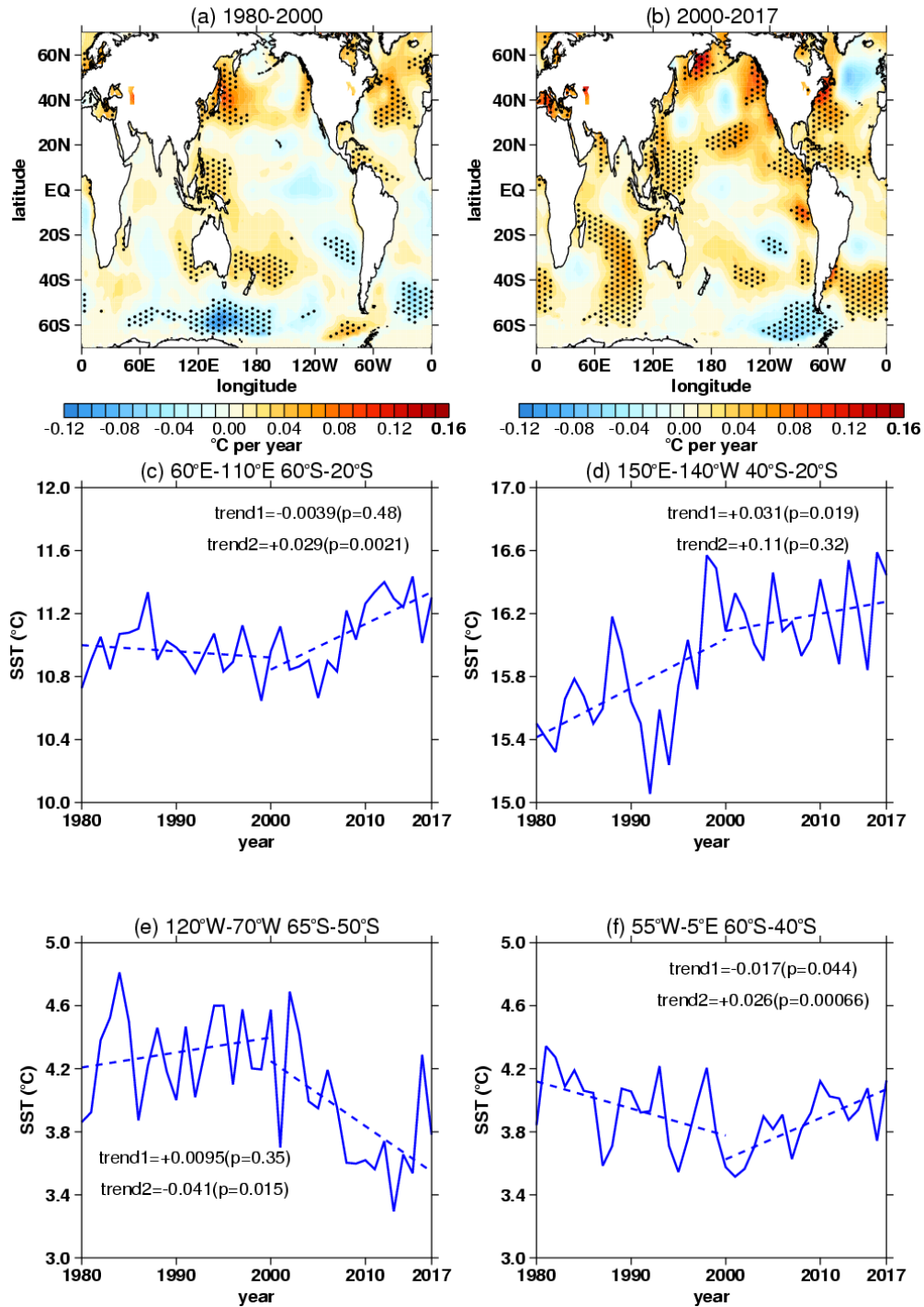
FIG. 8. Trends of SST in September over (a) 1980-2000 and (b) 2000-2017 derived

from ERSST v5 dataset. The stippled regions represent the trends significant at/above

the 90% confidence level. (c-f) Time series (blue solid lines) of SST during 1980-2017

over different regions (titles). The dashed lines represent linear regressions of SST time

series on piecewise periods (1980-2000 and 2000-2017). The "trend1" and "trend2"

1001 labeled in Figs. 8c-f represent the trend coefficients and the corresponding significances

1002 (bracketed) over 1980-2000 and 2000-2017, respectively.
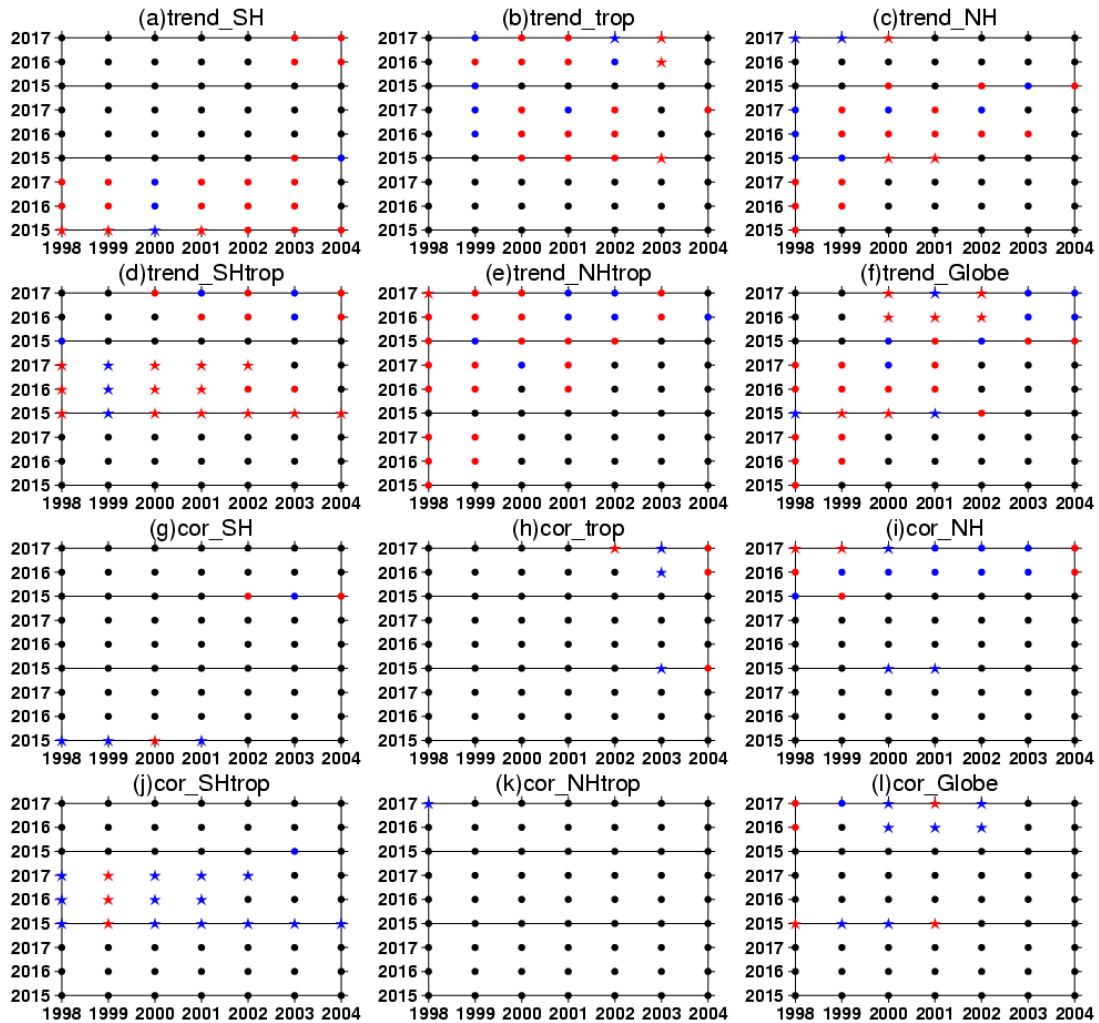
1003

1004 **FIG. 9.** Trend significance of the first three SST principal components (PCs) in (a) the

1005 extratropical southern hemisphere (SH, 70°S-20°S), (b) the tropics (TROP, 20°S-20°N),

1006 (c) the extratropical northern hemisphere (NH, 20°N-70°N), (d) the extratropical

1007 southern hemisphere and the tropics (SHtrop, 70°S-20°N), (e) the extratropical northern

1008 hemisphere and the tropics (NHtrop, 20°S-70°N), (f) the globe (70°S-70°N) and the

1009 corresponding (g, h, i, j, k, l) correlation significances between them and vertical E-P

1010 flux (Fz, area-weighted from 100 hPa to 30 hPa over 70°S-50°S) during different

1011 beginning years (x-axes) and ending years (y-axes). The red and blue dots indicate

1012 positive and negative trend or correlation coefficient are significant, respectively. The

1013 black dots indicate the trends or correlation coefficients are not significant. The stars

1014 indicate that the trends and the corresponding correlation coefficients are both

1015 significant. Each panel is divided into three regions from bottom to top, corresponding

1016 to the first, the second and the third principal components, respectively. The criterion

1017 to distinguish whether the trends and correlations are significant or not is the 90%

1018 confidence level.
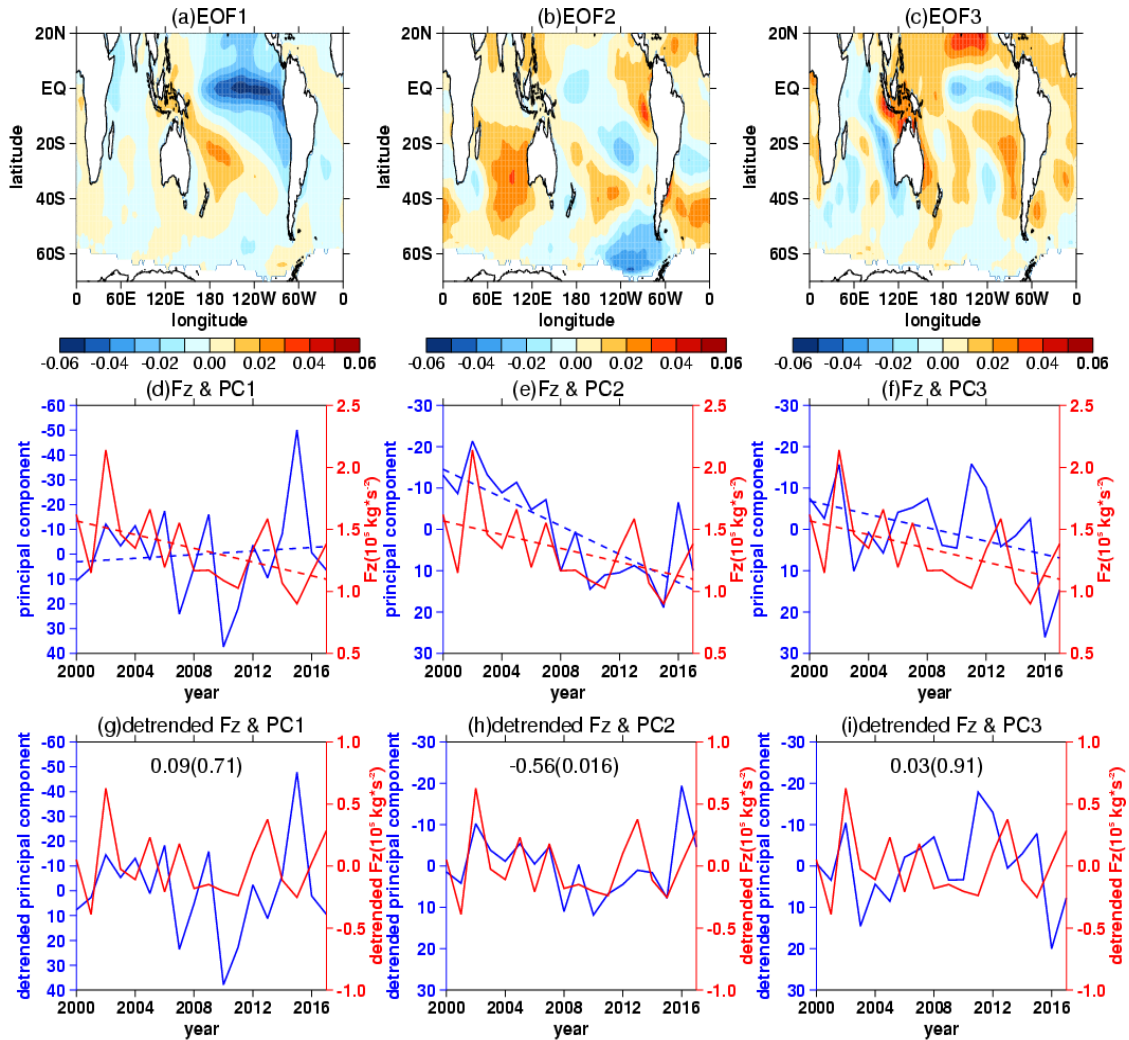
1019

1020 **FIG. 10.** (a, b, c) The first three EOF patterns of SST in SHtrop region. (d, e, f) The

1021 original time series of the first three principle components (PCs, blue solid lines

1022 correspond to left inverted y-axes) and stratospheric vertical E-P flux (Fz, area-

1023   weighted from 100 hPa to 30 hPa over 70°S-50°S, red solid lines correspond to right y-

1024   axes) in September during 2000-2017. The blue and red dashed lines in (d, e, f)

1025   represent the linear regressions of PC time series and Fz time series, respectively. The

1026   meaning of (g, h, i) are the same as (d, e, f) correspondingly, except the detrended time

1027   series. The unbracketed and bracketed numbers in (g, h, i) represent the correlation

1028   coefficients between detrended PC time series and Fz time series and the corresponding

1029   p values calculated by two-tailed t test, respectively.
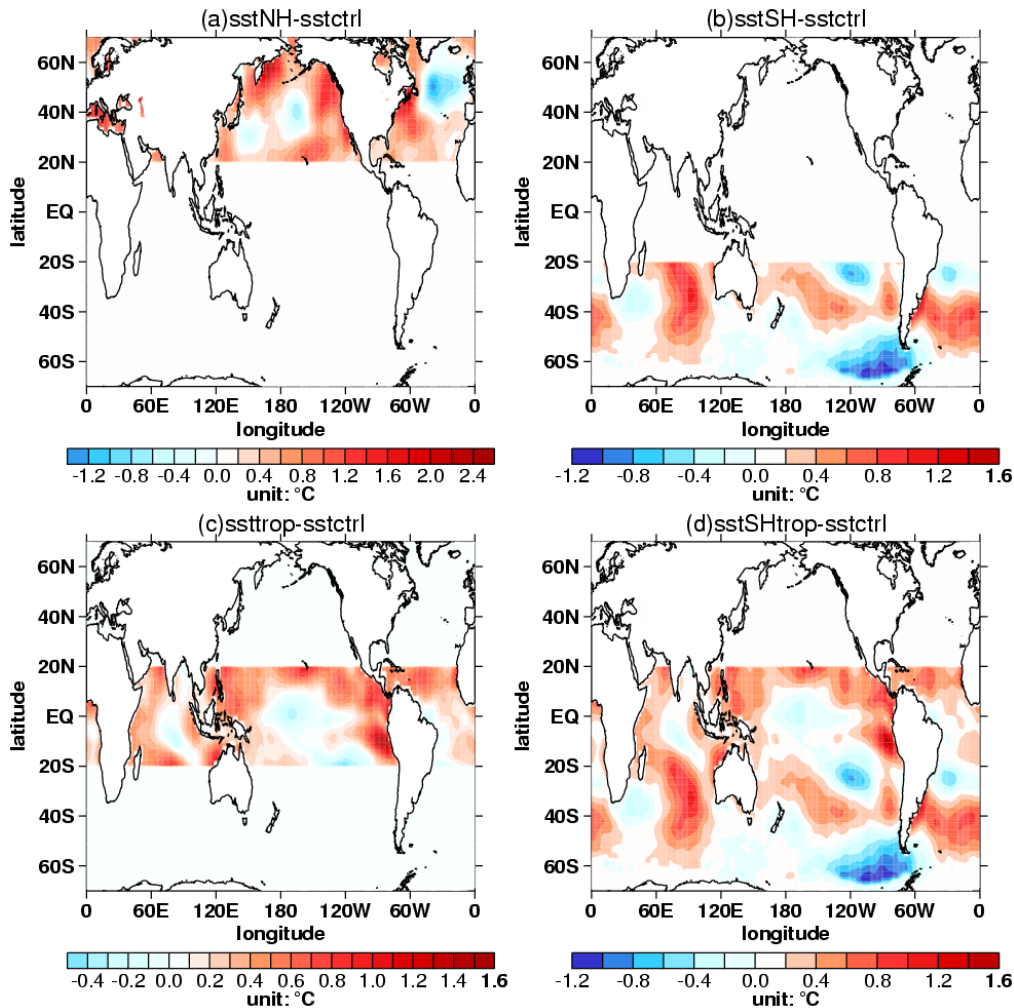
1030

1031   **FIG. 11.** Differences in SST forcing field between sensitive experiments ((a) sstNH; (b)

1032   sstSH; (c) ssttrop; (d) sstSHtrop) and the control experiment (sstctrl).
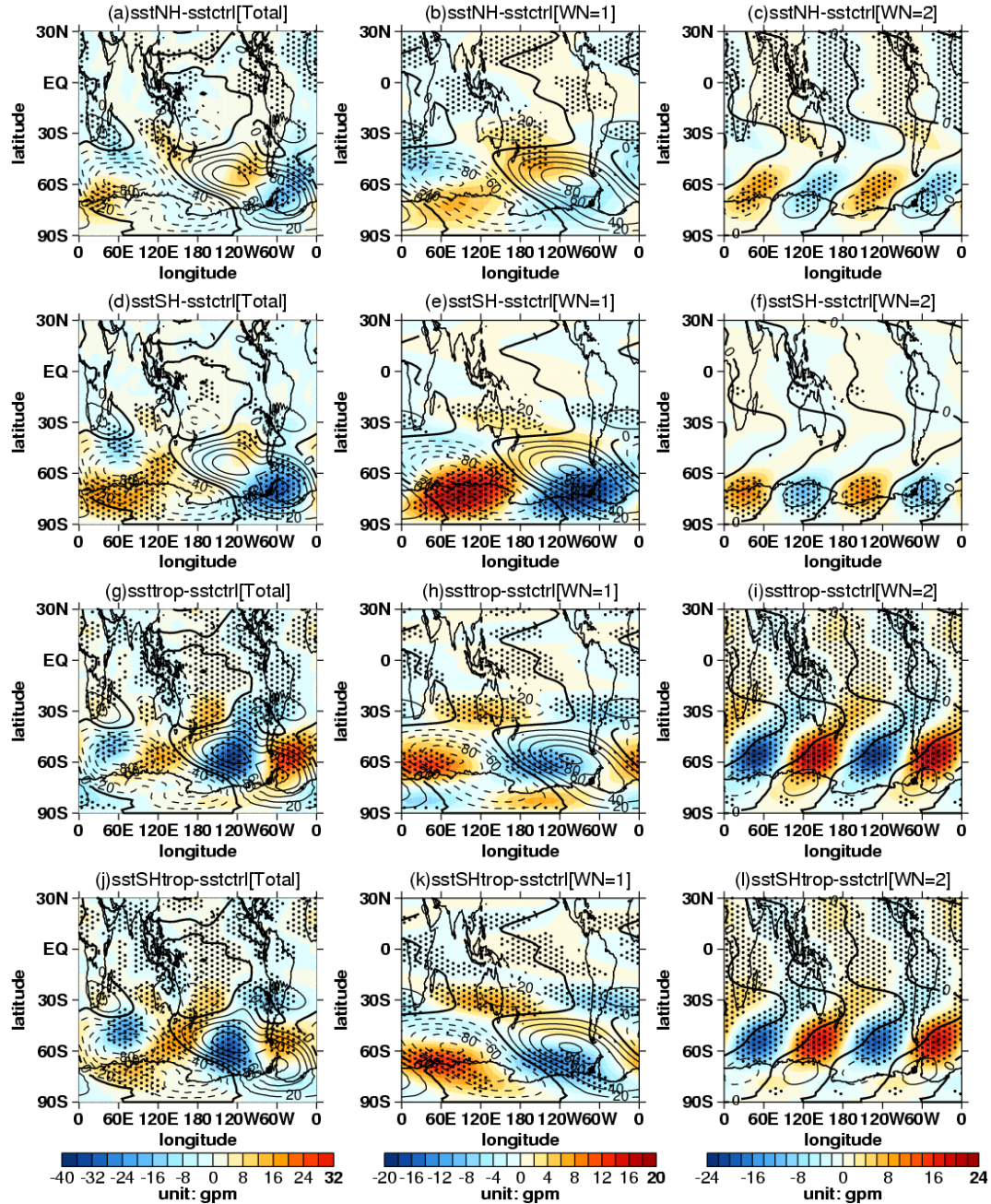
1033

FIG. 12. Differences (shadings) of (a, d, g, j) 500 hPa geopotential height zonal

deviations with their (b, e, h, k) wave-1 component and (c, f, i, l) wave-2 component

between sensitive experiments ((a, b, c) sstNH; (d, e, f) sstSH; (g, h, i) ssttrop; (j, k, l)

sstSHtrop) and the control experiment (sstctrl). The mean distributions (contours with

an interval of 20 gpm, positive and negative values are depicted by solid and dashed

lines respectively, zeroes are depicted by thick solid lines) of them are derived from the

 control experiment. The stippled regions represent the mean difference significant

 at/above the 90% confidence level.
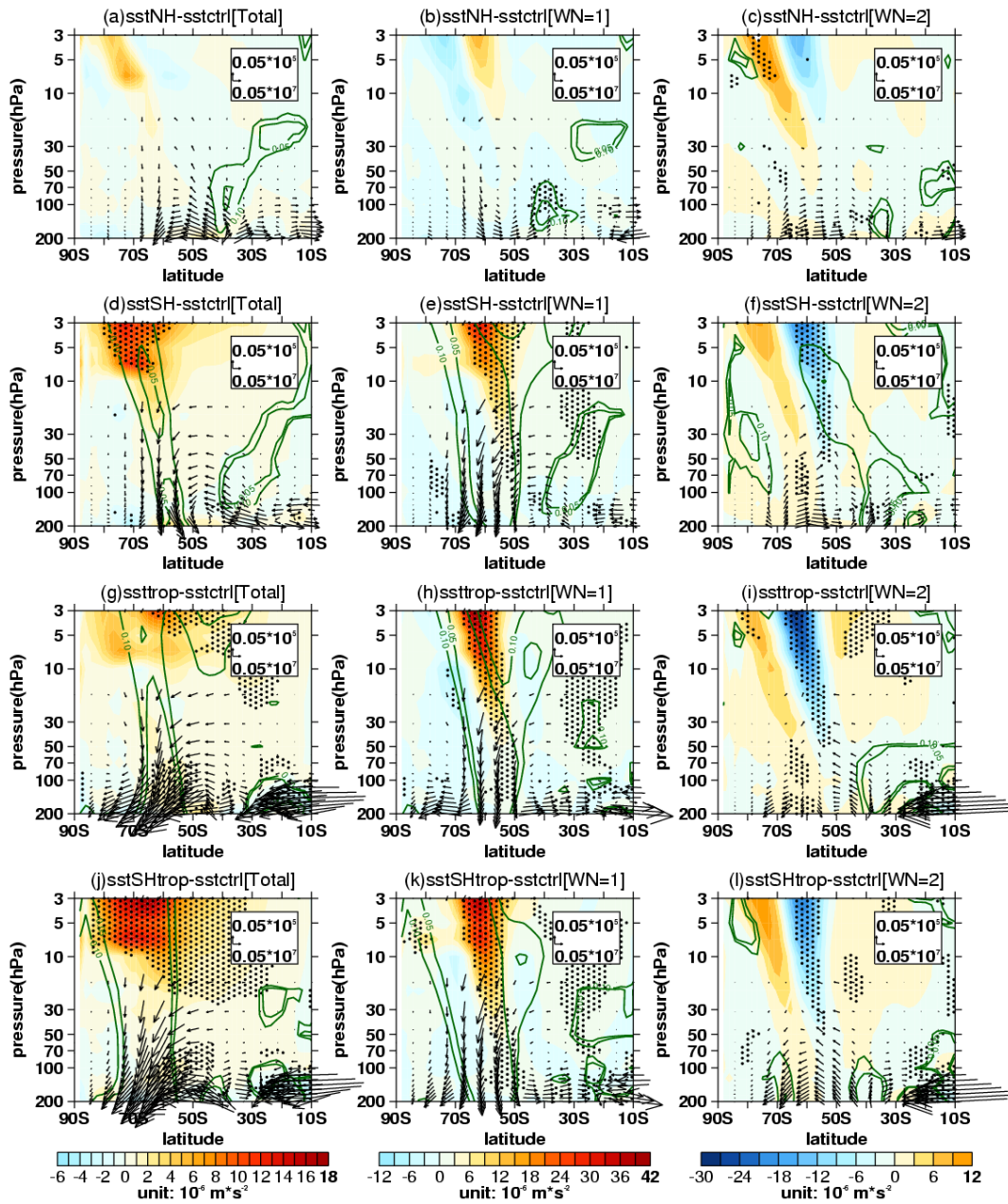
1042

FIG. 13. Differences of (a, d, g, j) stratospheric E-P flux (arrows, units in horizontal and vertical components are 0.05×10^7 and 0.05×10^5 kg·s^{-2}, respectively) and its divergence (shadings) with their (b, e, h, k) wave-1 component and (c, f, i, l) wave-2 component between sensitive experiments ((a, b, c) sstNH; (d, e, f) sstSH; (g, h, i) ssttrop; (j, k, l) sstSHtrop) and the control experiment (sstctrl). The stippled regions

1048   represent the mean differences of E-P flux divergence significant at/above the 90%

1049   confidence level. The green contours from outside to inside (corresponding to p=0.1,

1050   0.05) represent the mean differences of vertical E-P flux significant at the 90% and 95%

1051   confidence levels, respectively.
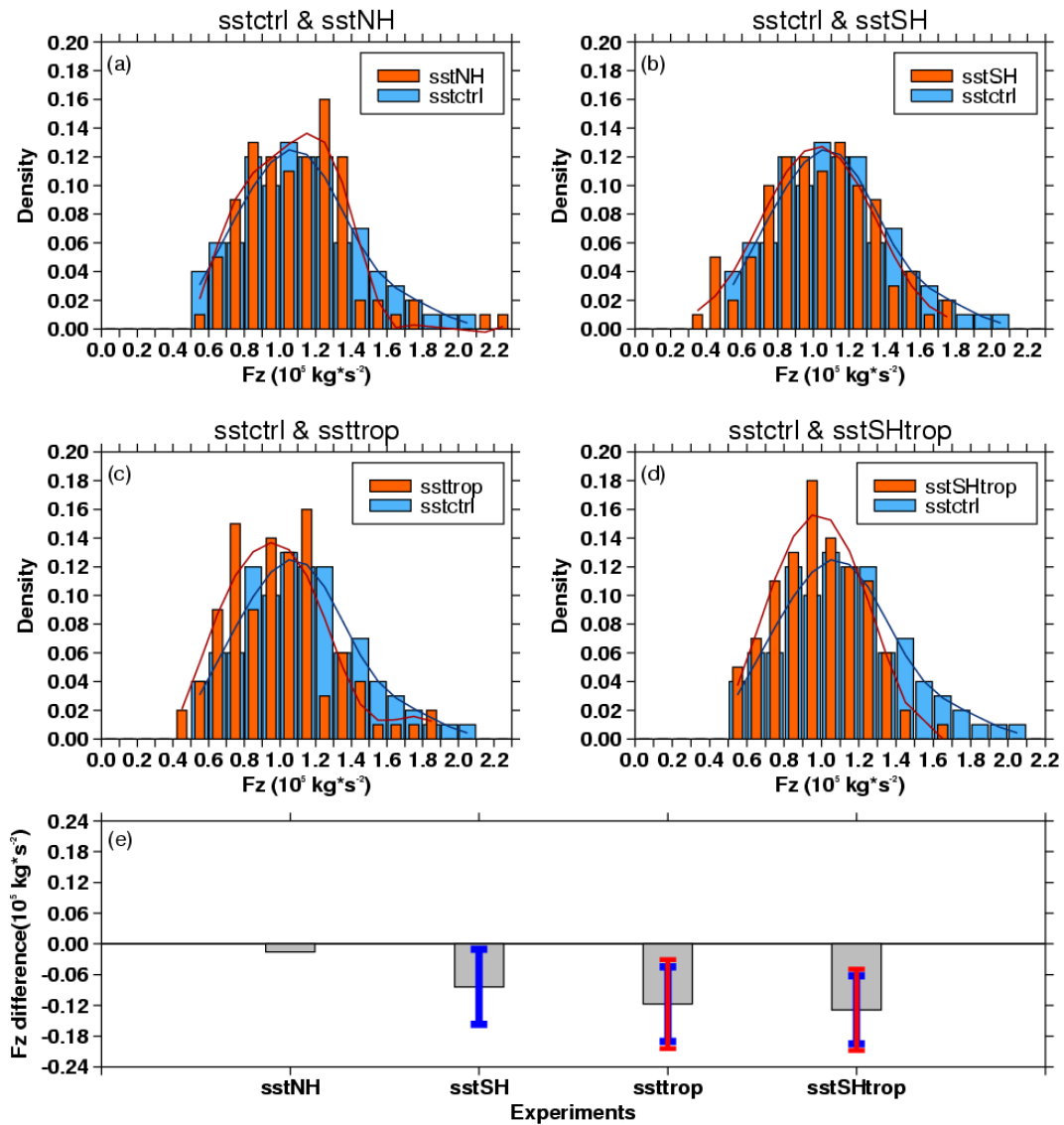
1052

1053   **FIG. 14.** (a, b, c, d) Frequency distributions (pillars, blue for control experiment and

1054   orange for sensitive experiments) of vertical E-P flux (Fz, area-weighted from 200 hPa

1055   to 10 hPa over 70°S-50°S) and its 5-point low-pass filtered fitting curves (solid lines,

1056   blue for control experiment and red for sensitive experiments) derived from 100

1057   ensemble members of the control experiment (sstctrl) and sensitive experiments ((a)

1058   sstNH; (b) sstSH; (c) ssttrop; (d) sstSHtrop), respectively. (e) Mean differences (grey

1059   pillars) and corresponding uncertainties (error bars) of Fz between sensitive

1060   experiments and the control experiment. The blue and red error bars reflect the 90%

1061   and 95% confidence levels calculated by two-tailed t test, respectively. The error bar is

1062   omitted when the significance of mean difference is lower than the corresponding

1063   confidence level.

1064
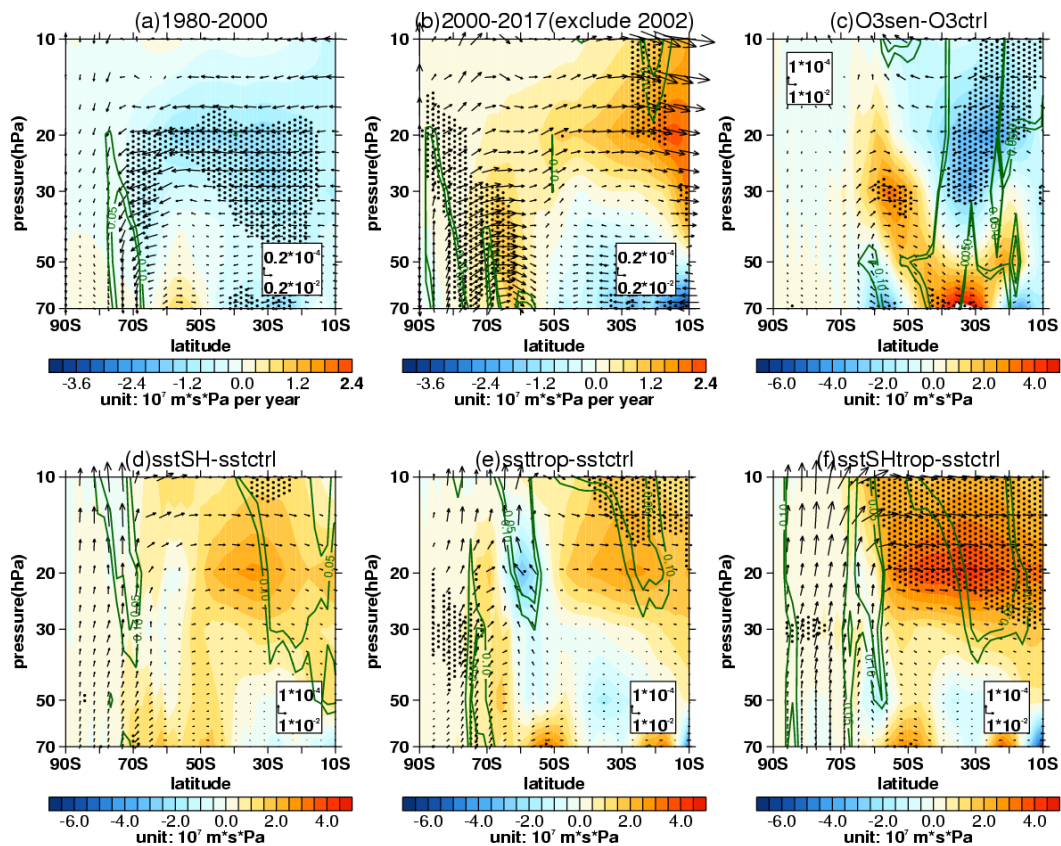
1065

1066   **FIG. 15.** (a) Trends of southern hemispheric Brewer-Dobson circulation (arrows, units

1067   in horizontal and vertical components are 0.2×10^{-2} and 0.2×10^{-4} m·s^{-1} per year,

1068   respectively) and its stream function (shadings) in September during (a) 1980-2000 and

1069   (b) 2000-2017 derived from MERRA-2 dataset. Data in 2002 are removed when trends

1070 are calculated in Figure (b). (c) Differences of Brewer-Dobson circulation (arrows,

1071 units in horizontal and vertical components are 10^{-2} and 10^{-4} m·s^{-1}, respectively) and its

1072 stream function (shadings) between the O3ctrl and O3sen. (d, e, f) Differences of

1073 Brewer-Dobson circulation and its stream function between the control experiment

1074 (sstctrl) and sensitive experiments ((d) sstSH; (e) ssttrop; (f) sstSHtrop) with SST

1075 changes. The stippled regions represent the trends or differences of the stream function

1076 significant at/above the 90% confidence level. The green contours from outside to

1077 inside (corresponding to p=0.1, 0.05) represent the trends or differences of the vertical

1078 components significant at the 90% and 95% confidence levels, respectively.